Check for updates

JGR Solid Earth

RESEARCH ARTICLE
10.1029/2026JB034241

Combining Borehole Seismic Data and Deep-Learning Methods to Monitor Seismic Sequences in the Istanbul-Marmara Region, NW Türkiye

Oliver Fabisch[1], **Marco Bohnhoff**[1,2], **and Patricia Martínez-Garzón**[1,3]

[1]GFZ Helmholtz Centre for Geosciences, Potsdam, Germany, [2]Free University Berlin, Institute of Geological Sciences, Berlin, Germany, [3]RWTH University of Aachen, Aachen, Germany

Key Points:

- Combined borehole and surface waveform processing with deep learning yields a refined catalog for six moderate Marmara sequences
- Borehole seismic arrays improve pick quality and phase associability and lower the magnitude of completeness in the near fault area
- Waveform similarity and template matching reveal sequence-dependent seismicity clustering and localization before mainshocks

Supporting Information:

Supporting Information may be found in the online version of this article.

Correspondence to:

O. Fabisch,
oliver.fabisch@gfz.de

Citation:

Fabisch, O., Bohnhoff, M., & Martínez-Garzón, P. (2026). Combining borehole seismic data and deep-learning methods to monitor seismic sequences in the Istanbul-Marmara region, NW Türkiye. *Journal of Geophysical Research: Solid Earth*, *131*, e2026JB034241. https://doi.org/10.1029/2026JB034241

Received 10 MAR 2026
Accepted 7 OCT 2026

Author Contributions:

Conceptualization: Oliver Fabisch, Marco Bohnhoff, Patricia Martínez-Garzón
Data curation: Oliver Fabisch
Formal analysis: Oliver Fabisch
Funding acquisition: Patricia Martínez-Garzón
Investigation: Oliver Fabisch
Methodology: Oliver Fabisch, Marco Bohnhoff, Patricia Martínez-Garzón

© 2026 The Author(s). Journal of Geophysical Research: Solid Earth published by Wiley Periodicals LLC on behalf of American Geophysical Union. This is an open access article under the terms of the Creative Commons Attribution License, which permits use, distribution and reproduction in any medium, provided the original work is properly cited.

Abstract The North Anatolian Fault Zone beneath the Sea of Marmara in NW Türkiye displays a 50% probability of an M $\geq$ 7 earthquake within the next decades. The proximity of the fault to the Istanbul megalopolis highlights the need for high-resolution microseismicity monitoring to identify seismicity transients including pre-mainshock clustering. We analyze six 4.0 $\leq M_L \leq$ 5.8 earthquake sequences in the eastern and central Marmara region from 2016 to 2023 and focus on the occurrence of seismicity immediately prior to the mainshocks. We combine borehole and surface seismic waveform data with deep-learning phase picking, automated phase association, and non-linear relocation to compile a comprehensive seismicity catalog. Compared with conventional processing, our workflow allows us to detect about eight times more events in time windows around the mainshocks in the area instrumented with borehole sensors. We then apply waveform cross-correlation, refined location techniques, and template matching to quantify waveform similarity and characterize seismic activity preceding moderate events. We observe a strong increase in waveform similarity and decrease in inter-event distance prior to a 2016 M_L 4.5 event in the Çınarcık Basin, consistent with earlier results from manual processing, and identify additional highly similar events preceding the mainshock. The 2019 M_L 5.8 Silivri sequence shows increased waveform similarity but more heterogeneous spatial clustering. We demonstrate that borehole seismic arrays are critical for resolving these subtle signals due to higher signal-to-noise ratios. Our workflow provides a robust basis towards near-real-time microseismic monitoring in the Istanbul-Marmara region and systematically identifying seismicity transients and localization processes.

Plain Language Summary The plate-bounding Main Marmara Fault (MMF) Zone beneath the Sea of Marmara in northwestern Türkiye runs close to the megacity Istanbul and is expected to produce a large earthquake in the coming decades. We study very small earthquakes around the fault to see whether they show patterns that may precede larger events. We analyze six earthquakes of magnitude 4.0–5.8 that occurred between 2016 and 2023 and examine the small earthquakes occurring beforehand. Processing high-quality borehole and surface seismic data with modern machine-learning techniques, we detect about eight times more earthquakes near the borehole network than contained in seismicity catalogs based on standard methods. We find increasingly similar earthquake signals and a tighter spatial cluster before a magnitude 4.5 earthquake in June 2016. September 2019 shows a more varied pattern, with similar events before its magnitude 4.7 event but no comparable spatial convergence toward the later magnitude 5.8 mainshock. The GONAF borehole network is crucial for seeing these subtle signals. Our results demonstrate the potential of combining borehole data with deep-learning methods to monitor the Main Marmara Fault shear zone hosting the potential to transfer our processing scheme to other seismic hazard hot spot regions.

1. Introduction

Low-magnitude earthquake detection and near-fault seismic monitoring are the key to decipher seismic deformation processes at small magnitude ranges, including seismicity transients or earthquake localization, potentially signifying impending hazardous earthquakes. This is of particular importance in seismically active areas that are co-located with metropolitan regions or critical infrastructure. The Sea of Marmara region in northwestern Türkiye is the most prominent seismic risk hot spot in greater Europe (Crowley et al., 2021), where the submarine segmented Main Marmara Fault shear zone (MMF, Le Pichon et al., 2001; Bohnhoff, 2026), as the northern and main branch of the North Anatolian Fault Zone (NAFZ), runs near the megalopolis Istanbul with its 18+ million inhabitants. A recurrence period of 250 years for M > 7 earthquakes along the MMF shear zone has been

Supervision: Marco Bohnhoff, Patricia Martínez-Garzón
Visualization: Oliver Fabisch
Writing – original draft: Oliver Fabisch
Writing – review & editing: Marco Bohnhoff, Patricia Martínez-Garzón

reported (Murru et al., 2016). With the last large earthquake having occurred in 1766, the MMF shear zone can be considered to be late in its seismic cycle and to have accumulated a substantial slip deficit. Consistent with this long-term perspective, scenario-based modeling indicates upper-bound magnitudes around $M_w \sim 7.1$ to 7.3 under a range of physically plausible assumptions, and up to $M_w \sim 7.4$ when additional stress perturbations from the 1912 Ganos/Murefte (M_w 7.4) and 1999 İzmit/Kocaeli (M_w 7.4) events (see Figure 1) are incorporated (Guvercin & Barbot, 2025; Öztürk et al., 2025). Statistical models indicate a 35%–70% probability for such an earthquake occurring by 2046 (Murru et al., 2016; Parsons, 2004), underscoring the urgent need for improved monitoring and subsequent potential warning capabilities, particularly because severe shaking is expected and may be amplified by fault geometry and directivity towards the coast of Istanbul (Chen et al., 2025; Martínez-Garzón et al., 2026; Öztürk et al., 2025).

A deterministic prediction of earthquakes (i.e., the precise timing, location, and magnitude of an event) is not yet possible and may remain unachievable (Beroza et al., 2021). However, laboratory experiments under acoustic monitoring and using machine-learning (ML) can identify subtle processes preceding failure of rock samples under controlled conditions (Rouet-Leduc et al., 2017). Further advancing these findings and transferring seismic processing technology from field to laboratory scale (Kwiatek et al., 2024) together with applying modern ML-approaches (Karimpouli et al., 2023, 2024) showed good progress in forecasting large-slip events in the lab. However, upscaling such approaches to the meso/reservoir (Karimpouli et al., 2025) and field (Delorey et al., 2021; Johnson & Johnson, 2021) scale showed that challenges remain towards forecasting larger ('run-away') induced or natural earthquakes. Earthquake preparation processes and precursors at the plate tectonic scale have proven to be hard to detect, inconsistent, highly variable or non-existent (e.g., Kanamori, 1981; Martínez-Garzón & Poli, 2024).

Foreshocks exemplify this challenge, as they precede only a subset of moderate to large earthquakes, with reported occurrence rates varying widely among studies depending on the adopted foreshock definition, catalog completeness, and spatial, temporal, and magnitude selection criteria (Abercrombie & Mori, 1996; Chen & Shearer, 2016; Jones & Molnar, 1979; Khan et al., 2025; Reasenberg, 1999; Trugman & Ross, 2019). Even in highly complete catalogs, estimated proportions change substantially when temporal fluctuations in background seismicity are included and when observed rate increases are tested against ETAS-type triggering (van den Ende & Ampuero, 2020; Moutote et al., 2021). Consequently, the physical relationship between foreshocks and mainshock nucleation remains debated (e.g., Gomberg, 2018; Helmstetter & Sornette, 2003; Kato & Ben-Zion, 2021; Martínez-Garzón & Poli, 2024; Mignan, 2014). Contrasting interpretations have also been proposed for sequences in the Marmara region. In particular, the preparatory phase of the 1999 İzmit earthquake has been attributed either to an extended nucleation process involving accelerating slow slip or to a cascade of triggered foreshocks (Bouchon et al., 2011; Ellsworth & Bulut, 2018). Discriminating between such competing interpretations requires detailed observations of the spatial and temporal evolution of low-magnitude seismicity, which can be provided by high-resolution earthquake catalogs (e.g., Cabrera et al., 2022; Cui et al., 2025).

Recent advances in machine learning, particularly deep learning, have substantially improved the construction of such catalogs (e.g., Woollam et al., 2022). Applications in phase picking (e.g., Mousavi et al., 2020; Ross et al., 2018; Zhu & Beroza, 2019) or phase association (e.g., McBrearty & Beroza, 2023; Zhu et al., 2022), among others, can lead to much more detailed and refined catalogs (Mousavi & Beroza, 2022). However, beyond these algorithms, hybrid workflows that combine DL phase picking with conventional processing (e.g., Isken et al., 2025) and conventional phase association algorithms (Münchmeyer, 2024) have also been substantially refined and show promising performance in recent benchmarks (Puente Huerta et al., 2025). These new methods, coupled with further increasing seismic network coverage, and in particular low-noise recordings in boreholes improving signal quality, have the potential to substantially improve the detection and characterization of low-magnitude seismicity and its spatial and temporal variability.

The Istanbul-Marmara region benefits from several permanent and temporary surface seismic networks that are complemented by borehole seismic arrays. The combination of regional surface stations with borehole sensors operating under low-noise conditions provides broad azimuthal coverage and has progressively improved catalog completeness and hypocentral resolution in the region (Becker et al., 2023a, 2023b; Kılıç et al., 2020; Martínez-Garzón, Beroza, et al., 2023; Wollin et al., 2018). However, the performance of advanced catalog-building methods remains constrained by the quality and temporal stability of the underlying observations.

21699356, 2026, 10, Downloaded from https://agupubs.onlinelibrary.wiley.com/doi/10.1029/2026JB034241 by Universitatsbibliothek RWTH Aachen University, Wiley Online Library on [05/11/2026]. See the Terms and Conditions (https://onlinelibrary.wiley.com/terms-and-conditions) on Wiley Online Library for rules of use; OA articles are governed by the applicable Creative Commons License

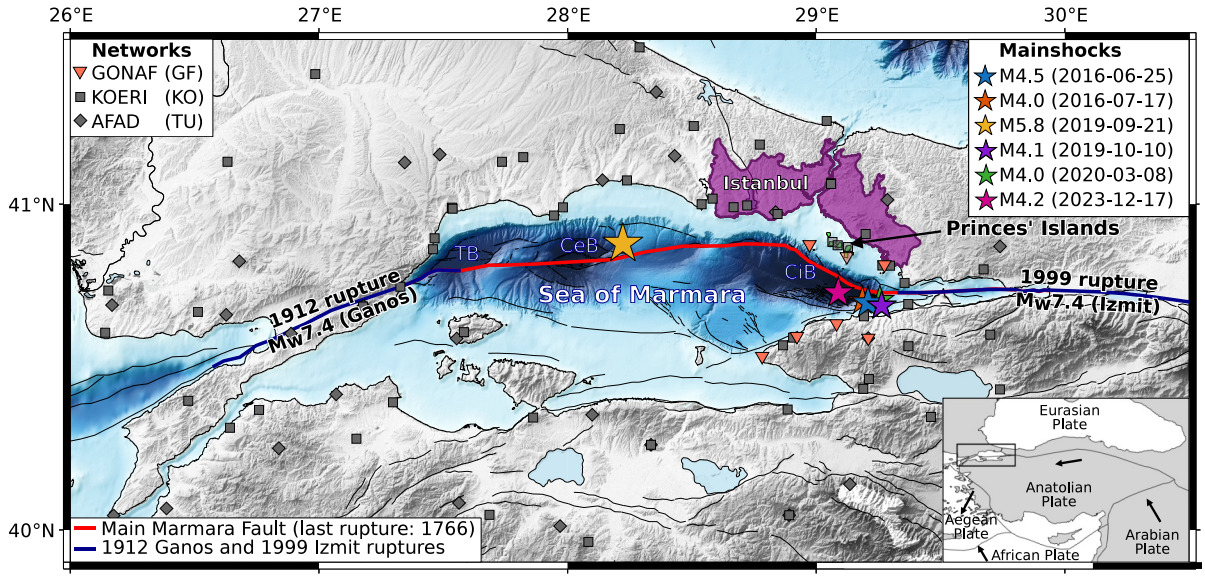


Figure 1. Tectonic setting and seismic monitoring infrastructure in the Sea of Marmara region. Blue lines mark the 1912 M_w 7.4 Ganos/Murefte and the 1999 M_w 7.4 İzmit/Kocaeli earthquakes. The red line shows the Main Marmara Fault shear zone (simplified). Colored stars denote the $4.0 \leq M_L \leq 5.8$ earthquake sequences analyzed in this study. TB: Tekirdağ Basin, CeB: Central Basin, CiB: Çınarcık Basin. Downward triangles indicate the borehole seismic arrays of the GONAF observatory (GF), squares and diamonds indicate KOERI (KO) surface stations and the Turkish National Seismic Network operated by AFAD (TU), respectively. Inset: Regional location map with arrows schematically indicating relative plate motions.

In this study, we analyze the six moderate earthquake sequences (M_L 4.0–5.8) that occurred from 2016 to 2023 in the proximity of the MMF shear zone beneath the Sea of Marmara. We use an enhanced detection, relocation, and cross-correlation workflow to improve seismicity catalogs. The results confirm and extend observations of pre-mainshock seismicity localization for a M_L 4.5 earthquake in June 2016 and resolve a more heterogeneous pattern of pre-mainshock clustering during the September 2019 M_L 5.8 Silivri sequence. We discuss the relevance and limitations of these observations by assessing what enhanced near-fault borehole monitoring can reveal about moderate earthquake sequences in the context of a potentially pending large earthquake in the region.

2. Regional Tectonic Framework

The Anatolian plate lies in a complex tectonic region within the active Mediterranean earthquake belt, where several major continental plates shaped the region's structure (e.g., Bozkurt, 2001). One of the most prominent features in this region is the NAFZ, which is a major right-lateral strike-slip system that separates the Anatolian and the Eurasian plate (Şengör, 1979; Şengör et al., 2005). The NAFZ extends approximately 1200 km from the Karlıova triple junction in eastern Türkiye to the northern Aegean Sea in the west (Bohnhoff et al., 2016; Şengör et al., 2005). The tectonic evolution and dynamics of the NAFZ are primarily controlled by two major forces, which are the northward push of the Arabian plate in the east (Bozkurt, 2001) and the southward rollback of the Hellenic subduction zone in southern Greece in the west (Flerit et al., 2004; Jolivet et al., 2013; Le Pichon et al., 2016). The latter most likely dominates the westward escape of Anatolia (Bulut et al., 2012; Flerit et al., 2004). While the slip rates remain relatively constant over much of the NAFZ's length at 20 mm/yr, they increase to 25 mm/yr in the Marmara region due to its interaction with the Aegean back-arc extension (Flerit et al., 2004; McClusky et al., 2000; Reilinger et al., 2006).

While the NAFZ shows a relatively narrow, well-defined fault trace along its eastern and central sections, it splits into several strands to the west as it enters the Marmara region (Bohnhoff et al., 2016; Le Pichon et al., 2016; Wong et al., 1995). The MMF shear zone, accommodates most of the deformation (Hergert & Heidbach, 2010; Reilinger et al., 2006) and runs close to Istanbul. It is segmented and crosses several deep basins: the Tekirdağ Basin in the west, the Central Basin, and the eastern Çınarcık Basin (Şengör et al., 2005, see Figure 1). The level of segmentation of the fault is still a matter of debate in the literature (e.g., Wollin et al., 2018; Şahin et al., 2022).

21699356, 2026, 10, Downloaded from https://agupubs.onlinelibrary.wiley.com/doi/10.1029/2026JB034241 by Universitatsbibliothek RWTH Aachen University, Wiley Online Library on [05/11/2026]. See the Terms and Conditions (https://onlinelibrary.wiley.com/terms-and-conditions) on Wiley Online Library for rules of use; OA articles are governed by the applicable Creative Commons License

21699356, 2026, 10, Downloaded from https://agupubs.onlinelibrary.wiley.com/doi/10.1029/2026JB034241 by Universitatsbibliothek RWTH Aachen University, Wiley Online Library on [05/11/2026]. See the Terms and Conditions (https://onlinelibrary.wiley.com/terms-and-conditions) on Wiley Online Library for rules of use; OA articles are governed by the applicable Creative Commons License

Recent seismological and geodetic studies have revealed varying fault behaviors along the MMF shear zone. While the Princes Island segment as the eastern part of the MMF shear zone had been identified to be locked based on the absence of microearthquakes and seismic repeaters down to depths of about 10 km (Bohnhoff et al., 2013) as well as GPS measurements (Ergintav et al., 2014), a different fault behavior was proposed towards the west. In the Central Basin (e.g., Schmittbuhl et al., 2016; Bohnhoff, Wollin, et al., 2017; R. Yamamoto et al., 2019) seismic repeaters indicating aseismic creep were observed. In contrast to neighboring locked segments in the east (Princes' Islands segment) and west of the MMF shear zone (onshore Ganos fault), this creeping section presumably exhibits aseismic creep accounting for 25%–75% of the local plate deformation (Bohnhoff, Wollin, et al., 2017), evidenced by a refined search for repeating earthquakes (Becker et al., 2023a, 2023b; Bohnhoff, Wollin, et al., 2017) and geodetic data (Y. Yamamoto et al., 2020). Analyzing the systematics of earthquake repeater groups indicative of aseismic fault creep, a systematic transitional fault behavior between the locked and creeping sections was identified along the MMF shear zone (Becker et al., 2023a, 2023b).

3. Observations of Seismicity Preceding Mainshocks in the Marmara Region

From a physical perspective, two commonly end-member interpretations for foreshock sequences are discussed (Ellsworth & Beroza, 1995). In cascade-type models, foreshocks are simply the earliest part of an aftershock-like triggering cascade described by Epidemic Type Aftershock Sequence statistics, without any special physics associated uniquely with the eventual mainshock (e.g., Helmstetter & Sornette, 2003; Mignan, 2014). In this view, the observed acceleration of seismicity, magnitude distributions and spatial migration of foreshocks can be reproduced if each earthquake is allowed to trigger further events, and the mainshock is just one realization of this branching process. In contrast, pre-slip nucleation models interpret at least part of the foreshock sequence as a manifestation of quasi-stable aseismic slip that gradually concentrates stress on a locked asperity until dynamic rupture initiates, as predicted by rate-and-state friction theory (e.g., Dieterich, 1992; Ruina, 1983) and supported by observations of repeating earthquakes and localized creep on some fault segments (e.g., Bohnhoff, Wollin, et al., 2017). Building on a global synthesis of foreshock and preparation processes, it is argued that these cascade and pre-slip models should be regarded as simplified end members and that real earthquake preparation typically involves a combination of both processes, modulated by local fault structure, loading conditions and external forcing. In this framework, clusters of highly similar small events that progressively localize and repeatedly rupture the same or closely neighboring patches are viewed as seismological tracers of an underlying aseismic loading process that may, in some cases, be superimposed on an otherwise cascade-like triggering background.

Such foreshocks have been observed for several notable earthquakes in the Istanbul-Marmara region. Reprocessing the (sparse) seismic waveform recording before the 1999 M_w 7.4 İzmit/Kocaeli earthquake allowed to detect several foreshocks in the hours preceding the mainshock (Bouchon et al., 2011; Ellsworth & Bulut, 2018). This observation triggered discussions on whether the occurrence of foreshocks might be a general phenomenon in the region. Based on improved low-noise recordings from the GONAF downhole observatory, a sequence of 18 events down to magnitude $M \sim 0.1$ was detected from manual picking, starting approximately 54 hr before the 2016 M_L 4.5 mainshock in the eastern Sea of Marmara (light blue star in Figure 1) (Malin et al., 2018). Furthermore, the seismicity before the mainshock had high pairwise cross-correlation coefficients (*ccc*) indicating a localization of seismicity in the immediate mainshock hypocenter area. In 2019, the M_L 5.8 Silivri earthquake (yellow star in Figure 1) that occurred at the central MMF shear zone was also preceded by seismicity, including a M_L 4.7 foreshock that itself had foreshocks (Durand et al., 2020). These sequences motivated the current study in which we performed a more detailed scanning of recent $M \geq 4.0$ earthquakes along the MMF shear zone, to investigate the systematic occurrence of immediate seismicity prior to mainshocks in the study region.

4. Data and Methods

4.1. Monitoring Networks and Earthquake Sequences

Seismicity in the Marmara region is monitored by several permanent regional and local seismic networks, including the GONAF borehole network (Bohnhoff, Dresen, et al., 2017; GFZ Helmholtz Centre For Geosciences & Disaster And Emergency Management Presidency, 2013), which enhances microseismic detection capabilities (Bohnhoff, Dresen, et al., 2017; Malin et al., 2018; Prevedel et al., 2015). The GONAF stations feature vertical arrays of seismometers installed at depths down to 300 m. This significantly reduces the noise and lowers the

Table 1
The Six Mainshock Sequences Investigated in this Study

Mainshock date	Location	M_w AFAD	M_w/M_L KOERI	Data range
2016-06-25	CiB	4.2	4.4/4.5	2016-06-22–2016-06-28
2016-07-17	CiB	3.9	4.1/3.9	2016-07-15–2016-07-20
2019-10-10	CiB	4.0	3.8/4.1	2019-10-07–2019-10-13
2020-03-08	CiB	3.9	3.8/4.0	2020-03-06–2020-03-11
2023-12-17	CiB	4.1	4.0/4.1	2023-12-15–2023-12-20
2019-09-26	CeB	5.8	5.7/5.7	2019-09-22–2019-09-29

CiB, Çınarcık Basin; CeB, Central Basin (see Figure 1).

Note. Event date, location, and magnitude from the AFAD and KOERI catalogs are provided together with the analyzed time window of continuous waveform data.

magnitude detection threshold (Bohnhoff, Dresen, et al., 2017). For this study, we used seismic stations from these three networks (see Figure 1) located within a boundary box for the region defined by latitude range 39.5°N–41.5°N and longitude range 26°–30°E. We selected all six earthquake sequences, which occurred in the proximity of the MMF shear zone between June 2016 and December 2023, with mainshock magnitudes ranging from M 4.0 to M 5.8, where magnitudes reported by AFAD and KOERI differ by up to 0.3 magnitude units, depending on the seismicity catalog and magnitude type (Table 1). Five of these sequences originated in the southeastern Sea of Marmara that is surrounded by GONAF arrays, within the Çınarcık Basin, at the transition from the 1999 İzmit rupture to the Princes' Islands segment. The sixth sequence corresponds to the September 2019 M_L 5.8 Silivri earthquake in the Central Basin (see Figure 1). For each sequence, we analyzed continuous waveform data covering approximately three days before and after the mainshock to characterize seismicity immediately before the mainshock, as well as the subsequent aftershock sequences (except the data for the September 2019 sequence covered 4 days before and three days after due to a preceding M_L 4.7 foreshock).

As reference data for our analysis, we merged information from three existing seismicity catalogs: (a) Becker et al. (2023a, 2023b), extending the reprocessed uniform Marmara seismicity catalog spanning 2006–2016 by Wollin et al. (2018) until 2020, (b) KOERI, and (c) AFAD. For the seismic sequence in 2023 we only merged the seismicity catalogs by KOERI and AFAD. The merged reference seismicity catalog then included 642 entries, of which 20 events were classified by KOERI as suspected explosions, which were subsequently removed. This resulted in a final reference catalog of 622 events with magnitudes ranging from M 0.6 to M 5.7 within the latitude range 39.5°–41.5°N and longitude range 26°–30°E for the analyzed sequences. Additionally, we evaluated our results with manual GONAF Teşvikiye array picks for a sequence in June 2016 by Malin et al. (2018).

4.2. Phase Picking

Due to the typically higher recall rates compared to other DL phase pickers (e.g., Jiang et al., 2021), we implemented PhaseNet (Zhu & Beroza, 2019) in our phase picking workflow. PhaseNet uses a U-Net-style convolutional neural network architecture (Ronneberger et al., 2015) to transform three-component seismograms into probability distributions indicating the likelihood of P-arrivals, S-arrivals, or noise at each time step. To deploy and compare different pre-trained PhaseNet variants in a consistent way, we used the SeisBench framework (Woollam et al., 2022), which provides standardized access to state-of-the-art seismological ML models and benchmark data sets. Within SeisBench, we tested different PhaseNet implementations, trained on data recorded at the Northern California Earthquake Data Center (Northern California Earthquake Data Center, 2014), the pretrained INSTANCE model (Michelini et al., 2021), and the STEAD-based pretrained model (Mousavi et al., 2019) (Text S1 and Figure S1 in Supporting Information S1). Ultimately, we selected the pre-trained PhaseNet variant based on Northern California Earthquake Data Center (2014) with a detection threshold of 0.3 for both P- and S-phases, as it provided the best balance between sensitivity and false detection rates in our study area. During this process we resampled all data due to different sampling rates (e.g., 500 Hz at GF; 100 Hz at KO and TU) to 100 Hz to ensure consistency.

21699356, 2026, 10, Downloaded from https://agupubs.onlinelibrary.wiley.com/doi/10.1029/2026JB034241 by Universitatsbibliothek RWTH Aachen University, Wiley Online Library on [05/11/2026]. See the Terms and Conditions (https://onlinelibrary.wiley.com/terms-and-conditions) on Wiley Online Library for rules of use; OA articles are governed by the applicable Creative Commons License

21699356, 2026, 10, Downloaded from https://agupubs.onlinelibrary.wiley.com/doi/10.1029/2026JB034241 by Universitatsbibliothek RWTH Aachen University, Wiley Online Library on [05/11/2026]. See the Terms and Conditions (https://onlinelibrary.wiley.com/terms-and-conditions) on Wiley Online Library for rules of use; OA articles are governed by the applicable Creative Commons License

4.3. Phase Association

We used PyOcto (Münchmeyer, 2024) for phase association. Unlike ML/DL methods, PyOcto uses a purely algorithmic phase association approach based on a 4D space-time partitioning strategy inspired by an octotree-like data structure to identify seismic events from phase picks. Although we also tested the GaMMA (Zhu et al., 2022), we ultimately chose PyOcto for our final analysis, because its superior performance in our environment, particularly through higher recall rates, consistent with other studies (e.g., Puente Huerta et al., 2025), and fewer duplicate/split events as stated in different in previous studies (e.g., Becker et al., 2024; Martínez-Garzón, Becker, et al., 2023).

An event was required to contain at least six phase picks, with at least three different stations, each contributing both a P- and an S-pick. We also set the minimum node size to 10.0 and used a location node size of 1.5 for final hypocenter determination. Additional parameters included a 300 s overlap between time slices to prevent missing events at segment boundaries, a pick matching tolerance of 1.5 s, and a minimum inter-event time of 3.0 s to distinguish closely spaced earthquakes. For travel-time calculations, we used a layered velocity model (Text S2 and Figure S2 in Supporting Information S1) that combines elements from Karabulut et al. (2011) and Becker et al. (2023a, 2023b), since PyOcto does not currently support continuous velocity gradients (as of 2025).

4.4. Earthquake Location and Magnitude Calibration

We located all PyOcto associated events using the NonLinLoc software package (Lomax et al., 2000, 2014). Hypocenters were calculated in a Lambert Conformal Conic projection centered on the study region with the same velocity model as used for phase association. Locations were obtained with the oct-tree search strategy combined with the Equal Differential Time method weighted by origin time. We required a minimum of six P- or S-phases per event, respectively, and we applied a two-step relocation procedure, in which a first NonLinLoc run preliminary locations and empirical station corrections were solved, which were then held fixed in a second pass in order to reduce systematic travel time biases.

Local magnitudes were calculated using the regional western Türkiye M_L scale of Kılıç et al. (2017). Amplitudes were extracted from Wood–Anderson simulated displacement waveforms after instrument-response removal using poles and zeros after Bormann and Dewey (2014). Full details are provided in Text S4 of the Supporting Information S1.

Finally, we retained only events with RMS ≤ 0.4 and maximum horizontal uncertainty $\leq$10 km (Figures S7 and S8a–S8c in Supporting Information S1) and removed events coinciding with KOERI entries classified as suspected explosions as in the construction of the merged reference seismicity catalog (see Section 4.1).

4.5. Relative Relocation, Waveform Cross-Correlation Analysis, and Template Matching

Waveform cross-correlation is a key method for quantifying the similarity of seismograms and for estimating relative time shifts between phases with sub-sample precision, which directly improves differential time measurements and relative earthquake locations (Schaff et al., 2004). It has become a standard tool to identify highly similar or repeating earthquakes along plate boundary faults, for example, at Parkfield on the San Andreas Fault and in the Sea of Marmara, where nearly identical waveforms indicate repeated activation of the same fault patches (e.g., R. M. Nadeau & McEvilly, 2004; Bohnhoff, Wollin, et al., 2017; Abercrombie et al., 2020; Waldhauser & Schaff, 2021). In discrete form the normalized cross-correlation function $c(\tau)$ can be written as (e.g., Grund et al., 2016)

$$c(\tau) = \frac{\sum_{i=1}^{n} u_1(t_i)\ \ u_2(t_i+\tau)}{\sqrt{\sum_{i=1}^{n} u_1(t_i)^2}\ \sqrt{\sum_{i=1}^{n} u_2(t_i)^2}}, \tag{1}$$

where $u_1(t_i)$ as well as $u_2(t_i)$ denote the discrete amplitudes of the seismograms at sample times t_i, while τ is the discrete time lag. The cross-correlation coefficient (ccc) is defined as the maximum value of $c(\tau)$ over all tested τ for a given station and component.

We used GrowClust3D.jl (Trugman et al., 2022; Trugman & Shearer, 2017), a hierarchical clustering algorithm that utilizes waveform cross-correlation differential travel times, to improve relative locations. Unlike double-

21699356, 2026, 10, Downloaded from https://agupubs.onlinelibrary.wiley.com/doi/10.1029/2026JB034241 by Universitatsbibliothek RWTH Aachen University, Wiley Online Library on [05/11/2026]. See the Terms and Conditions (https://onlinelibrary.wiley.com/terms-and-conditions) on Wiley Online Library for rules of use; OA articles are governed by the applicable Creative Commons License

difference methods based on global matrix inversion, GrowClust3D.jl progressively merges and relocates clusters of similar earthquakes using a graph-based approach. Relative locations are determined through an iterative grid search that minimizes the L1 norm of differential travel-time residuals.

Relocation was performed for two sequences on the full multi-period catalog within a 20 km radius of their respective mainshocks. Candidate pairs were selected from events separated by at most 6 km in 3D catalog space. Waveforms were resampled to 100 Hz, demeaned, linearly detrended, tapered, and band-pass filtered from 3 to 25 Hz using a zero-phase fourth-order filter. Correlation windows started 0.5 s before each phase pick and extended 1.0 s for P phases on vertical components and 1.5 s for S phases on horizontal components with the highest *ccc*. Normalized cross-correlations were computed over a maximum lag of ±0.30 s. The peak was refined to subsample precision using a three-point parabolic interpolation, and accepted measurements required $ccc \geq 0.6$ as well as a signal-to-noise ratio (SNR) ≥ 2.0. Location uncertainties were estimated using the bootstrap method implemented in GrowClust3D.jl, resampling cross-correlation differential times with replacement for 1,000 realizations and reporting the resulting median absolute deviations.

For later cross-correlation analysis, we used a variable window length approach based on twice the S-P time difference (Bohnhoff, Wollin, et al., 2017), which adjusts the correlation window to the event distance and travel time, making it particularly effective for identifying clusters of similar events across varying source-receiver geometries.

We defined a sequence-specific event subset by selecting all relative relocated events within 5 km of the respective mainshock epicenter. Waveforms were preprocessed following the same procedure used for the relative relocation. Then, for each sequence, we generated correlation matrices showing pairwise *ccc* values between events. Additionally, we calculated running averages of *ccc* values, including the standard error of the mean (SEM), and average inter-event distances using different sliding windows to identify potential temporal trends in waveform similarity.

To increase detection sensitivity before each mainshock in the Çınarcık Basin, we applied single-station template matching to continuous waveform data using EQcorrscan (Chamberlain et al., 2017). Details of template selection, preprocessing, detection parameters, quality control, and magnitude recalibration are provided in Text S5 of the Supporting Information S1.

5. Results

5.1. Phase Picking Performance of Borehole and Surface Installations

PhaseNet detected a total of 467,842 P- and S-phases across all earthquake sequences analyzed. The model detected a P- to S-wave pick ratio of 1.08, with 243,911 P-wave phases and 223,931 S-wave phases. The average pick probability was approximately 0.51. The cumulative numbers of picks and located events for the six sequences are shown in Figure 2.

For validation against manual picks, we compared our PhaseNet picks with an available data set for the June 2016 M_L 4.5 sequence at the deepest sensor of the nearest GONAF array (see Malin et al. (2018) for details). With our workflow we detected 55 P-wave phases and 51 S-wave phases out of 62 P-wave and 62 S-wave manual picks in Malin et al. (2018) within a tolerance window of ±0.5 s. Therefore, we can reproduce ∼89% of the P-wave picks and ∼82% of the S-wave picks with our routine.

The associated picks show a diurnal periodicity, with a day-to-night ratio of 1.46 for local working hours (8 a.m.–8 p.m.). The effect is weaker for GONAF borehole channels (1.30) than for surface stations (1.49). However, event-level day-night ratios are additionally controlled by sequence timing, as four of six mainshocks occur during the defined daytime interval (Figures S3a–S3d in Supporting Information S1).

The aftershock sequences provide a natural test case to compare differences in detection and association performance between surface installations and borehole sensors (Figures 3a and 3b). We stack all six sequences over the 30-hr-long window after each mainshock and normalize pick rates by the number of active sensors per sequence. This shows that surface stations generate pick rates per sensor ∼1.3 times higher than the borehole sensors, whereas borehole sensors provide 1.5 times more associated picks per sensor than the surface sensors during phase association (Figure 3a).

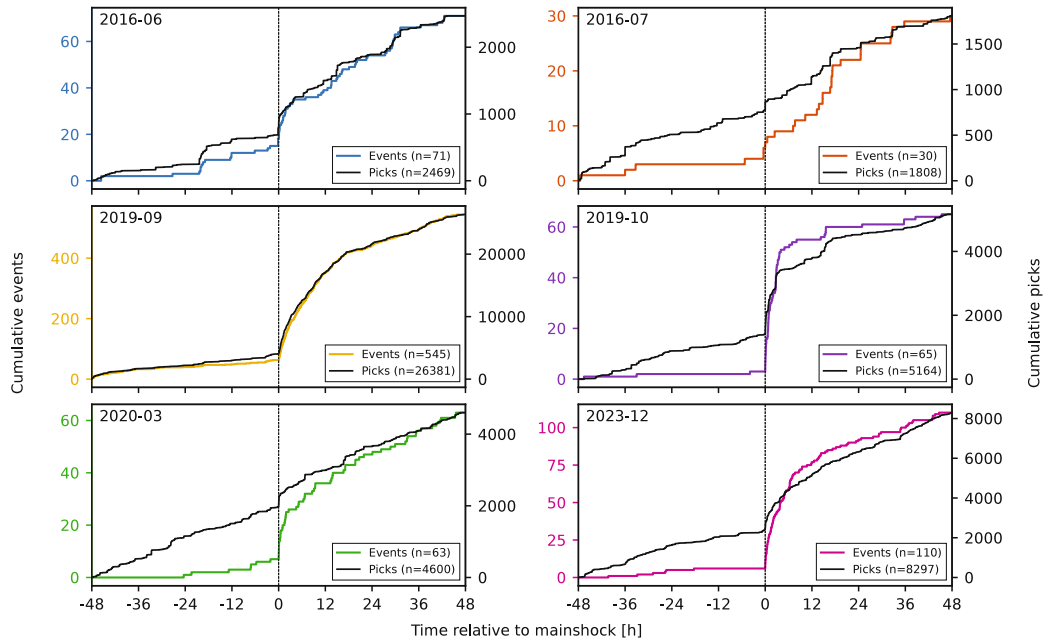


Figure 2. Cumulative number of events and picks as a function of time relative to the mainshock for the six investigated sequences. Each panel shows the cumulative count of located events within a radius of 20 km (colored lines, left *y* axis) together with the cumulative number of all generated picks in the same space time window (black lines, right *y* axis). Mainshock origin times are marked with vertical lines.

To quantify how pick association evolves with time after the mainshock, we define the cumulative pick-to-association efficiency as

$$E(t) = \frac{N_{\text{assoc}}(t)}{N_{\text{picks}}(t)}, \tag{2}$$

where $N_{\text{picks}}(t)$ is the cumulative number of picks and $N_{\text{assoc}}(t)$ the cumulative number of picks assigned to events within a time window of length t relative to the mainshock time in hours. In terms of temporal evolution, $E(t)$ reaches 71.2% for surface and 81.7% for borehole stations immediately after $t = 0$, but decreases to 55.8% and 69.9% within the first hour. When integrating over the full 30 hr time window, these values further decrease to 26.4% and 52.6%, corresponding to unassociated pick fractions of 73.6% for surface stations and 47.4% for

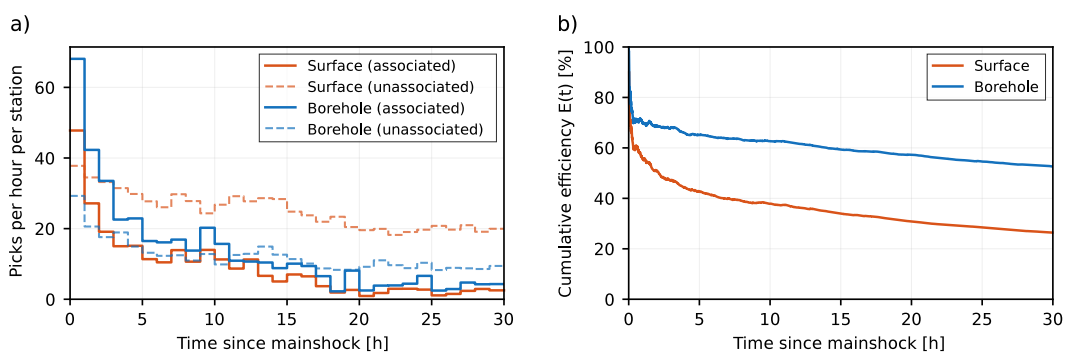


Figure 3. Pick statistics from borehole and surface stations following all mainshocks. (a) Number of picks per hour and station relative to the mainshock, separated by station type and usage: solid and dashed lines represent picks that were used and not used in the subsequent association process, respectively, with red for surface stations and blue for borehole sensors. (b) Cumulative detection efficiency $E(t)$, defined as the percentage of associated picks over time for surface stations and borehole sensors, respectively.

21699356, 2026, 10, Downloaded from https://agupubs.onlinelibrary.wiley.com/doi/10.1029/2026JB034241 by Universitatsbibliothek RWTH Aachen University, Wiley Online Library on [05/11/2026]. See the Terms and Conditions (https://onlinelibrary.wiley.com/terms-and-conditions) on Wiley Online Library for rules of use; OA articles are governed by the applicable Creative Commons License

21699356, 2026, 10, Downloaded from https://agupubs.onlinelibrary.wiley.com/doi/10.1029/2026JB034241 by Universitatsbibliothek RWTH Aachen University, Wiley Online Library on [05/11/2026]. See the Terms and Conditions (https://onlinelibrary.wiley.com/terms-and-conditions) on Wiley Online Library for rules of use; OA articles are governed by the applicable Creative Commons License

borehole sensors (Figure 3b). This decrease is mainly due to a decaying aftershock rate while PhaseNet continues to trigger on noise transients and other non-earthquake arrivals, particularly at noisier surface stations. This is also supported by station-noise measurements. Full-spectrum PSD estimates, compared with the Peterson (1993) noise models, show that surface stations have systematically higher noise levels and day-night noise contrast than borehole sensors at frequencies above ∼1 Hz (Figures S4–S6 in Supporting Information S1).

The sequence-wise statistics further reveal systematic differences between the Çınarcık Basin sequences near the borehole arrays and the more distant Central Basin sequence. In the Çınarcık Basin, surface stations often produce an order of magnitude more picks than borehole stations, but a much smaller fraction of these surface picks is retained during phase association, with 9.4% of surface picks associated compared to 37.0% of borehole picks within the previously defined 0–30 hr time window. For the 2019 M_L 5.8 sequence in the Central Basin, where both sensor types are located at larger epicentral distances, the efficiencies of both sensor types increase, but borehole sensors still outperform surface stations, with ∼69% of borehole picks associated compared to ∼52% for surface picks. Across all Çınarcık Basin sequences, borehole sensors contribute 3.2 to 4.5 times as many associated picks per active sensor, with the largest contrast in March 2020 and December 2023, and across the full data set and all events, the associated pick fraction is 12.6% for surface stations and 31.7% for borehole sensors, corresponding to about 2.5 times higher association likelihood overall for borehole sensors.

5.2. Seismicity Preceding M > 4 Earthquakes

We obtained a catalog with a total of 2,644 earthquakes. When compared against the reference catalog, 89% of the reference events within the study area (see Figure 1) were matched, and even 93% when focusing specifically on events within the Sea of Marmara. When narrowing the focus to the central and eastern Sea of Marmara region, the recall increases to 95%. For events with $M > 2$, all except one of the events were identified, with the missing event likely being a false detection after visual inspection.

Hypocentral depths are concentrated in the upper crust, with a median depth of 6.5 km. The median horizontal and vertical uncertainties are about 1.2 and 2.5 km, respectively (Figures S8c and S8d in Supporting Information S1). After applying quality-control criteria and removing suspected explosions, a total of 1,958 events remained in the catalog, which is about three times more events than in the reference catalog (Figure S7 in Supporting Information S1). The calibrated values for M_L are in the range $[-0.7, 5.8]$ (Figure 4e). Using the maximum curvature method for the frequency-magnitude distribution (Wiemer & Wyss, 2000; Woessner & Wiemer, 2005), the magnitude of completeness of our catalog is $M_c = 1.80$, compared to $M_c = 1.90$ in the reference catalog (Figures S19a and S20a in Supporting Information S1). The full-area estimate reflects the disproportionate contribution of the September 2019 M_L 5.8 Silivri sequence, which accounts for 833 of the 1,958 events in our catalog and is located predominantly outside the GONAF monitoring area (Figures 4c–4e). When restricting the seismicity catalog to the eastern Sea of Marmara area surrounded by the GONAF arrays (see Figure 1), the magnitude of completeness decreases to $M_c = 0.90$, compared with $M_c = 1.9$, thus showing one unit of magnitude decrease within the area covered by borehole-based monitoring (Figures 4a–4d; Figures S19b and S20b in Supporting Information S1). However, the events below $M_c = 0.90$ within the GONAF monitoring area are constrained by only a limited number of stations and therefore tend to have larger magnitude uncertainties. Representative filtered vertical-component waveforms spanning the catalog magnitude range are shown in Figures S9–S18 in Supporting Information S1.

In the Çınarcık Basin, the mainshocks of June and July 2016 (M_L 4.5, 4.0), October 2019 (M_L 4.1), March 2020 (M_L 4.0), and December 2023 (M_L 4.2) are all located within approximately 15 km of each other (Figures 5a, 5b, and 5d–5f). Despite their proximity, the sequences show variability in the number, timing, and spatial distribution of events preceding and following the mainshocks. The June 2016 M_L 4.5 mainshock was preceded by a localized cluster (22 events; M_L 0.3–3.7) within ∼54 hr, mostly within ∼1 km of the epicenter. Aftershocks in the following 24 hr (33 events; M_L 0.2–2.9) extended over a wider area but remained strongly clustered near the epicenter. By contrast, the remaining Çınarcık Basin sequences show lower pre-mainshock seismicity rates. During the available ∼50 hr pre-mainshock window, the July 2016 M_L 4.0 mainshock was preceded by five events within 10 km (M_L 0.1–2.6) and was followed by nine events within the first 24 hr (M_L 0.1–2.8) at distances of up to ∼9.8 km. No events occurred within 5 km of the October 2019 M_L 4.1 mainshock during the available pre-mainshock window. Within the first 24 hr after the mainshock, 56 aftershocks (M_L 0.3–3.8) occurred within 5 km, with 93% located within 2 km. The March 2020 M_L 4.0 mainshock was preceded by six events within

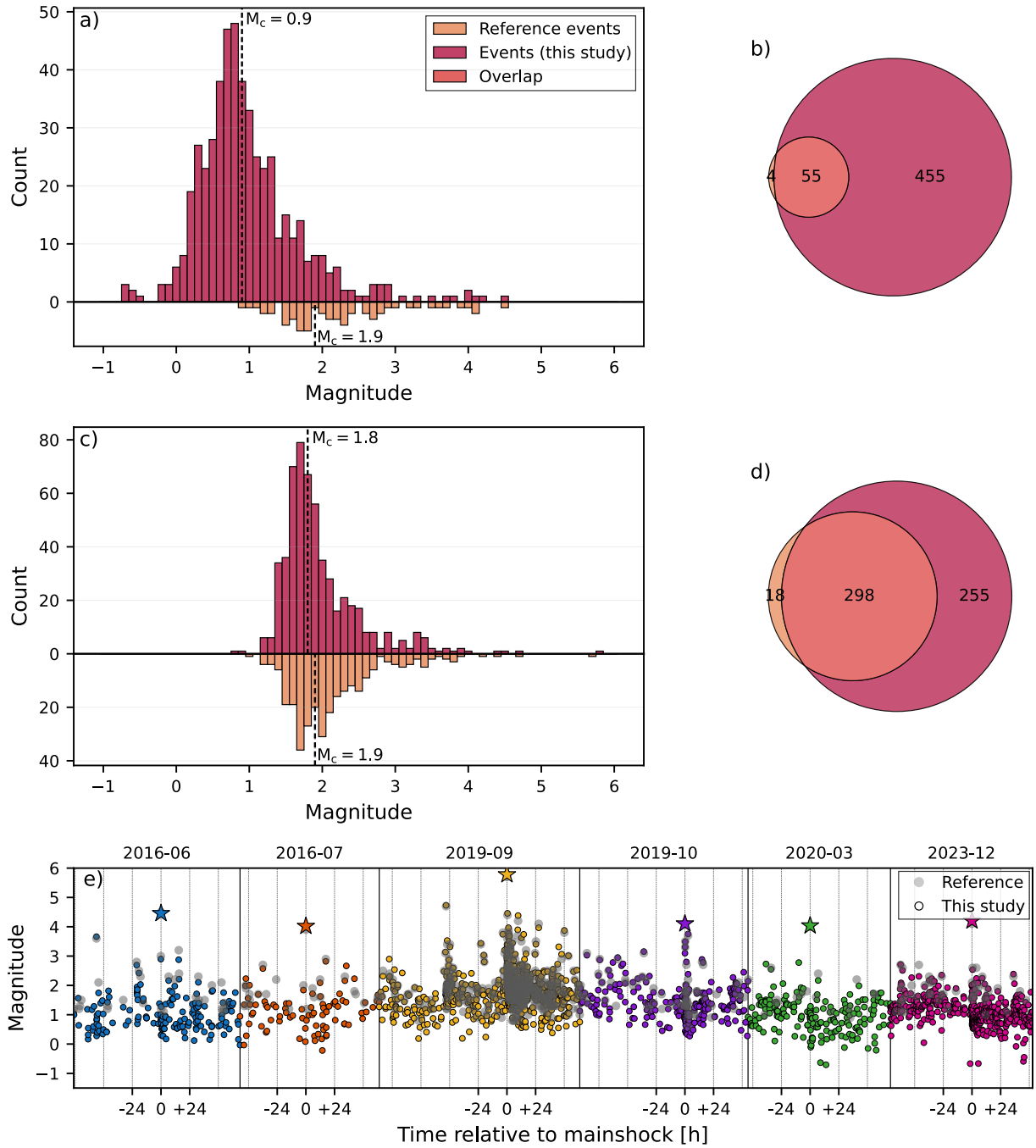


Figure 4. Comparison of magnitude distributions, catalog overlap, and temporal magnitude patterns between the catalog of located events in this study and the merged reference catalog. (a) Frequency-magnitude distributions for events in the Çınarcık Basin surrounded by the GONAF arrays (+10 km buffer) derived in this study (red bars) and the reference catalog (orange bars). Bars are binned at $\Delta M = 0.1$. Black dashed vertical lines mark the M_c estimated independently for each catalog. (b) Venn diagram of catalog overlap for the region in a; events are counted as common when a one-to-one spatiotemporal match exists ($|\Delta t| \leq 5$ s and epicentral distance ≤ 15 km). (c) and (d) Same as (a) and (b) for the Central Basin sequence (September 2019), defined as events within 10 km of the M_L 5.8 September 2019 mainshock epicenter in the reference catalog, showing only a minor M_c change ($M_c = 1.8$ computed vs. $M_c = 1.9$ reference). (e) Magnitude-time evolution of all computed events in this study as a function of relative time within each of the six mainshock sequences; gray dashed lines indicate 24 hr intervals, colors denote monthly sequences, grey dots denote the reference events, and black vertical lines separate sequences along the *x*-axis.

9.5 km (M_L 0.2–1.0), occurring in two brief episodes 2 days and 7 hr before the mainshock. The December 2023 M_L 4.2 mainshock was preceded by three events within ~3 km (M_L 1.0–1.7). Both sequences were followed by aftershock activity around the mainshocks.

21699356, 2026, 10, Downloaded from https://agupubs.onlinelibrary.wiley.com/doi/10.1029/2026JB034241 by Universitatsbibliothek RWTH Aachen University, Wiley Online Library on [05/11/2026]. See the Terms and Conditions (https://onlinelibrary.wiley.com/terms-and-conditions) on Wiley Online Library for rules of use; OA articles are governed by the applicable Creative Commons License

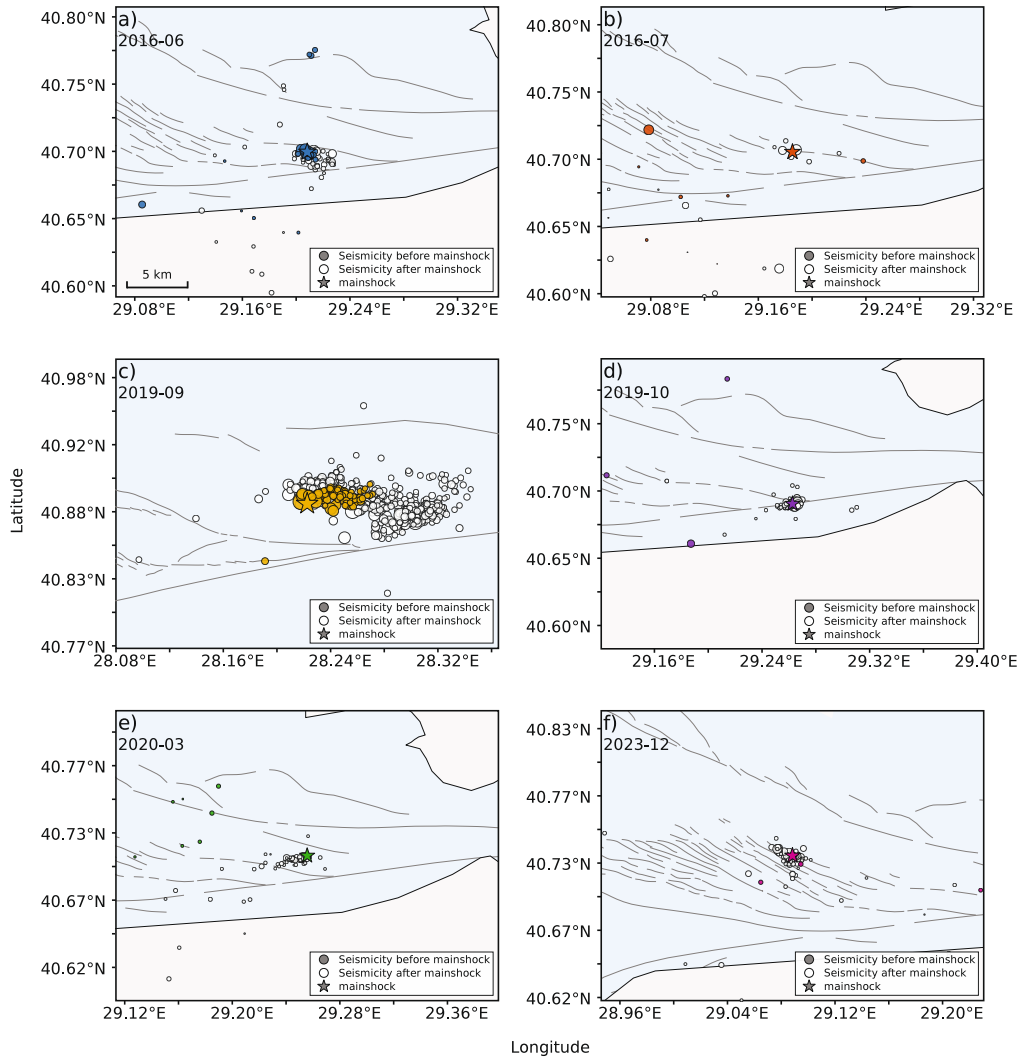


Figure 5. Mainshock-centered views of the seismicity sequences in 24 × 24 km boxes around the respective mainshock epicenters. Panels show the sequences of (a) June 2016, (b) July 2016, (c) September 2019, (d) October 2019, (e) March 2020, and (f) December 2023. Colored circles mark seismicity before the mainshock origin time, white circles indicate seismicity after the mainshock, and stars denote the mainshocks.

The Central Basin sequence with the M_L 5.8 Silivri mainshock, is associated with higher seismicity rates in the days leading up to and following the mainshock (Figure 5c). In 4.5 days preceding the mainshock, 102 events occurred (M_L 0.9 to 4.7), most of them up to 3 km away from mainshock. The largest foreshock reached M_L 4.7 and occurred about 51 hr before the mainshock, only 0.4 km away. Following the mainshock, 478 aftershocks (M_L 0.8 to 4.5) were located at median epicentral distance of 4.8 km.

5.3. Quantifying Seismicity Localization for Earthquake Sequences in the Çınarcık Basin

The events from the June 2016 M_L 4.5 Çınarcık Basin sequence form a spatially compact cluster, in terms of both the relative and the absolute hypocenter locations (Figures 5a and 6b). The clearest waveform similarity is observed at the deepest GONAF Teşvikiye borehole sensor, GF.TESV.01, located at 300 m depth and at an epicentral distance of ∼12.8 km (Figure 6a; Figure S21a in Supporting Information S1). The cross-correlation matrix is therefore restricted to the 41 events that were both detected and retained at this sensor, and comprises 10 and 30 events before and after the mainshock, respectively, plus the mainshock itself. Overall waveform similarity is moderate, with a median pairwise *ccc* of about 0.28. However, the matrix contains several localized high-similarity pairs, with maximum values reaching 0.94. Across all event pairs, *ccc* increases with decreasing

21699356, 2026, 10, Downloaded from https://agupubs.onlinelibrary.wiley.com/doi/10.1029/2026JB034241 by Universitatsbibliothek RWTH Aachen University, Wiley Online Library on [05/11/2026]. See the Terms and Conditions (https://onlinelibrary.wiley.com/terms-and-conditions) on Wiley Online Library for rules of use; OA articles are governed by the applicable Creative Commons License

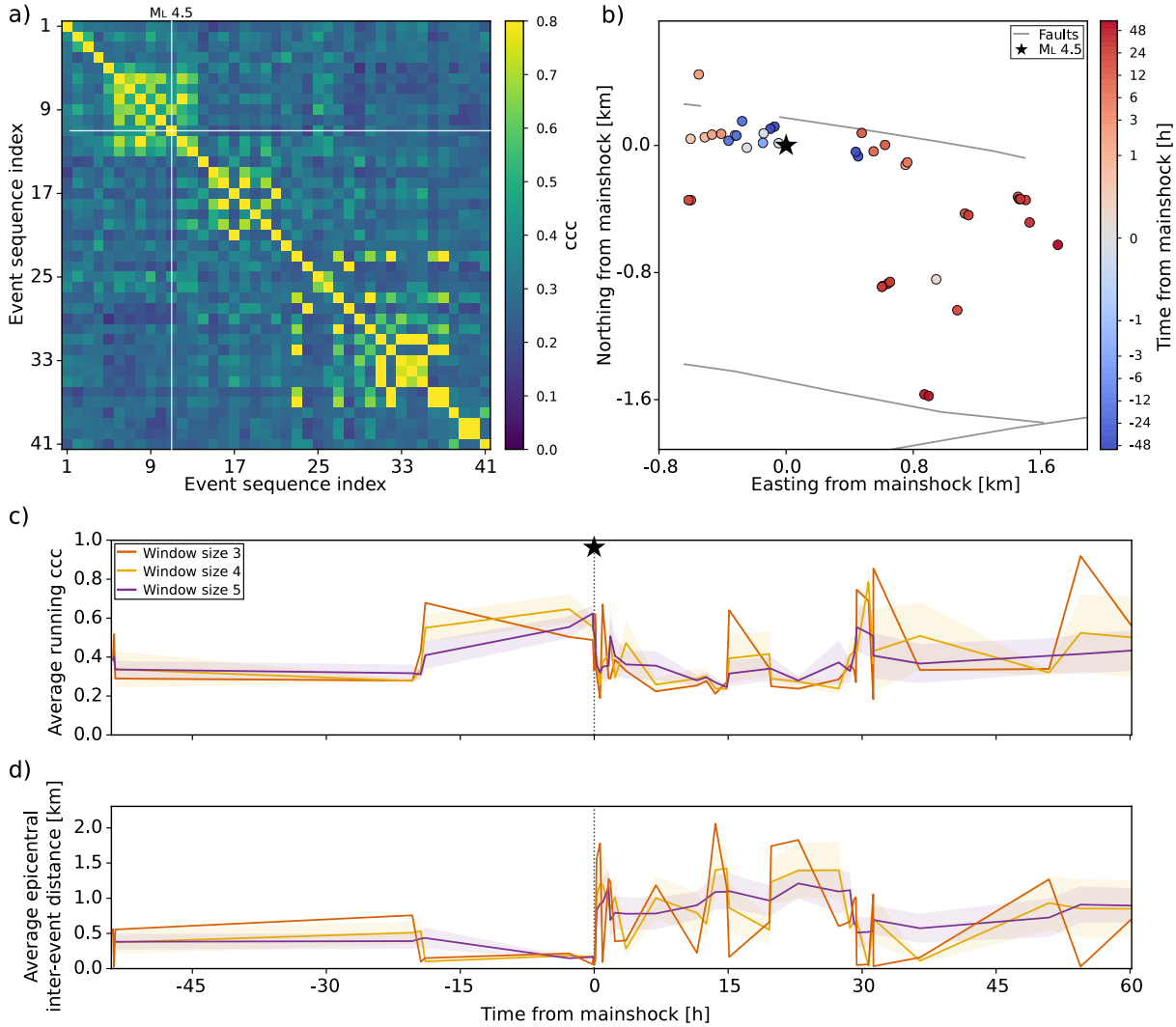


Figure 6. Waveform cross-correlation and relative locations for the M_L 4.5 June 2016 Çınarcık Basin sequence. (a) Cross-correlation matrix for 41 events detected at the borehole sensor GONAF-GF.TESV.01, ordered by origin time. The mainshock is marked in the matrix. (b) Epicentral distribution of relocated events, color encoded with time to mainshock. (c) Running average *ccc* for event windows of 3, 4, and 5 events. Shaded areas indicate mean ± SEM. (d) Running average epicentral inter-event distance for the same event windows as in (c).

epicentral separation, whereas time separation and magnitude difference show no comparably strong relationship. The most similar events occur during the final ~20 hr before the mainshock. In this interval, five events form a compact group closer to the mainshock and showing elevated waveform similarity with *ccc* values reaching about 0.76 with a median of about 0.66 (Figures 6c and 6d). The two earliest events in this group occur at distances of 316 and 364 m from the mainshock, respectively, whereas the final three events occur within 161 m, including the last event at only 49 m. All of these event pairs overlap within bootstrap uncertainties, and four of the five events prior to the mainshock overlap with it; the only exception is separated from the mainshock by 363 m, slightly exceeding the horizontal bootstrap uncertainty.

In contrast, the remaining four Çınarcık Basin sequences show limited seismic activity preceding the mainshocks (Text S5 and Figures S24–S28 in Supporting Information S1).

5.4. Quantifying Seismicity Localization in the 2019 M_L 5.8 Silivri Earthquake Sequence

At the deepest GONAF GF.TESV borehole sensor, 264 relative relocated events were detected (Figure 7c), including 58 and 205 events before and after the mainshock, respectively. The sequence shows a more

21699356, 2026, 10, Downloaded from https://agupubs.onlinelibrary.wiley.com/doi/10.1029/2026JB034241 by Universitatsbibliothek RWTH Aachen University, Wiley Online Library on [05/11/2026]. See the Terms and Conditions (https://onlinelibrary.wiley.com/terms-and-conditions) on Wiley Online Library for rules of use; OA articles are governed by the applicable Creative Commons License

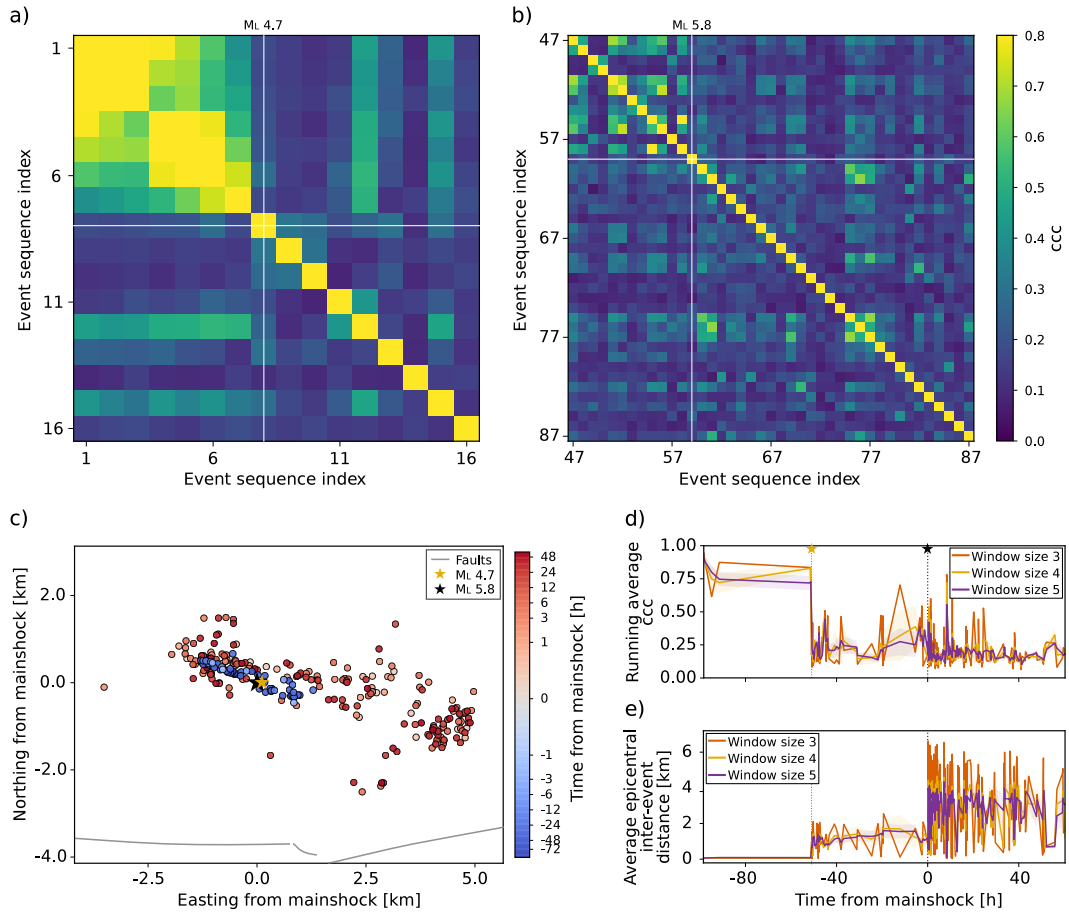


Figure 7. Waveform cross-correlation and relative locations for the September 2019 Central Basin sequence recorded at GONAF-GF.TESV.01. (a) Cross-correlation matrix for the first 16 events of the sequence, spanning the period around the largest foreshock (M_L 4.7). (b) Cross-correlation matrix for the 41-event mainshock window from 21.9 hr before to 1.0 hr after the M_L 5.8 mainshock. (c) Relative event locations for all 264 events included in the matrix and detected by GONAF-GF.TESV.01. The M_L 4.7 and M_L 5.8 events are shown by orange and the black stars, respectively. (d) Running average *ccc* for event windows of 3, 4, and 5 events. (e) Running-average epicentral interevent distance for the same windows. Shaded areas indicate mean ± SEM.

heterogeneous waveform similarity pattern than the June 2016 sequence, with median off-diagonal *ccc* of 0.16 (Figures 7a–7d; Figure S22 in Supporting Information S1).

The most pronounced pre-mainshock waveform family occurs before the M_L 4.7 foreshock. Seven events preceding the M_L 4.7 event, from ∼53 hr to 22 min before its occurrence, show high waveform similarity with a median pairwise *ccc* of 0.69 and a maximum of 0.94 (Figures 7a–7e). Their epicentral separations range from ∼40–364 m and all but two pairs overlap within the bootstrap uncertainties. No clear spatial shift towards the M_L 4.7 event is observed and four events overlap horizontally with the M_L 4.7 event within uncertainties.

The M_L 4.7 event itself is epicentrally close to the later mainshock (Figure 7c), at an epicentral distance of ∼110 m, but the waveform similarity is low ($ccc = 0.17$). The last 12 events before the M_L 5.8 mainshock occur between ∼22 and 1.5 hr before the mainshock and are located 0.36–1.34 km from the mainshock epicenter. These events do not show a monotonic approach toward the mainshock. Pairwise waveform similarity within this final event group is moderate, with a median *ccc* of 0.23 and a maximum of 0.83 (Figures 7b–7d). As a group, however, the final events prior to the mainshock are not tightly co-located with the mainshock and the waveform cross-correlations between them and the mainshock have a maximum *ccc* of 0.24.

21699356, 2026, 10, Downloaded from https://agupubs.onlinelibrary.wiley.com/doi/10.1029/2026JB034241 by Universitatsbibliothek RWTH Aachen University, Wiley Online Library on [05/11/2026]. See the Terms and Conditions (https://onlinelibrary.wiley.com/terms-and-conditions) on Wiley Online Library for rules of use; OA articles are governed by the applicable Creative Commons License

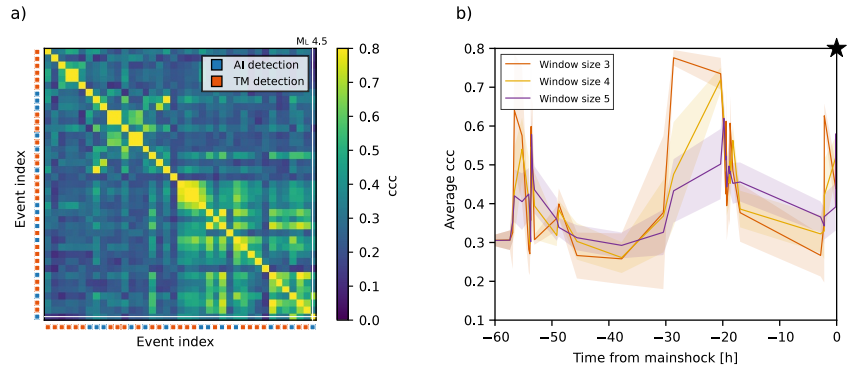


Figure 8. Waveform similarity matrix for catalog events and template detections at the deepest sensor of borehole station GF.TESV for the M_L 4.5 June 2016 sequence. (a) Normalized *ccc* for 39 waveform windows composed of 13 catalog events with SNR ≥ 3 (event index blue) within 3 km epicentral distance of the mainshock and 26 single-station template detections (event index orange), ordered chronologically up to the mainshock. The white horizontal and vertical lines mark the mainshock row and column. (b) Running average of pairwise *ccc* using window sizes of 3, 4, and 5 consecutive events. Shaded areas indicate mean ± SEM, and the black star marks the mainshock time.

5.5. Catalog Template Matching for Sequences in the Çınarcık Basin

To further examine the seismicity before the mainshocks, we apply template matching to the five sequences in the Çınarcık Basin, taking advantage of the borehole arrays located close to the epicenters. For the June 2016 sequence, template matching at the nearest GONAF borehole sensors reveals the clearest and most interpretable pattern of pre-mainshock detections. At GF.TESV.01, 39 detections span ∼66 hr up to the mainshock (Figures 8a and 8b; Figure S23 in Supporting Information S1), with an increase in detection density toward the mainshock (Figure 9a). A pronounced increase in running average *ccc* is observed ∼29 hr before the mainshock (Figure 8b), ∼9 hr earlier than with the methods used before, reaching a maximum average value of about 0.78 for the three-event window. Elevated average values of up to about 0.72 are also observed around 20 hr before the mainshock. For a catalog-based comparison, restricting to catalog events located within 5 km of the mainshock, the union of

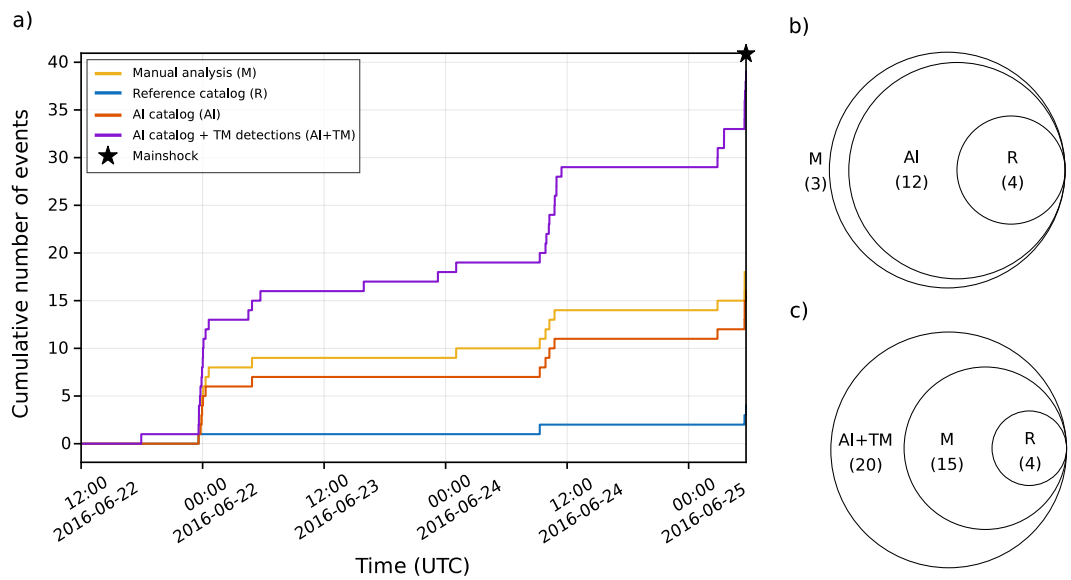


Figure 9. Comparison of manual, reference, AI, and single-station template matching catalogs for the June 2016 M_L 4.5 sequence with epicenters within 5 km distance to the mainshock. (a) Cumulative number of events as a function of origin time up to the mainshock (black star) for the manual analysis (M) (Malin et al., 2018), the merged reference catalog (R), the AI based catalog (AI), and the union of AI events and GF.TESV.01 (deepest sensor) template detections (AI + TM). The manual sequence comprises 19 events, 16 events are detected in the AI catalog, whereas the reference catalog lists only 4 events in this space–time window. (b) and (c) Venn diagram summarizing set overlaps.

21699356, 2026, 10, Downloaded from https://agupubs.onlinelibrary.wiley.com/doi/10.1029/2026JB034241 by Universitatsbibliothek RWTH Aachen University, Wiley Online Library on [05/11/2026]. See the Terms and Conditions (https://onlinelibrary.wiley.com/terms-and-conditions) on Wiley Online Library for rules of use; OA articles are governed by the applicable Creative Commons License

21699356, 2026, 10, Downloaded from https://agupubs.onlinelibrary.wiley.com/doi/10.1029/2026JB034241 by Universitatsbibliothek RWTH Aachen University, Wiley Online Library on [05/11/2026]. See the Terms and Conditions (https://onlinelibrary.wiley.com/terms-and-conditions) on Wiley Online Library for rules of use; OA articles are governed by the applicable Creative Commons License

the AI catalog and the GF.TESV.01 template matching detections recovers all 19 events manually identified by Malin et al. (2018) and all 4 events in the merged reference catalog, while contributing 20 additional detections not present in either catalog (Figures 9a–9c). The highest contributing templates are located <1 km away from the mainshock, and the magnitudes of the new events are predominantly small, with a median $M_L = 0.55$. Across the GF.TESV borehole array (at depths of 75, 150, 225, and 300 m, respectively), a cross-station coincidence check using station detection times as an origin time proxy identifies 19 multi-sensor event clusters (at least two sensors). Overall, 56 of 77 detections across TESV.01, TESV.02, TESV.03, and TESV.05 fall into these multi-station clusters, showing that most detections correspond to events visible across the array.

Template matching did not reveal comparably similar event families in the other nearby sequences. July 2016 October 2019, and December 2023 produced only sparse or weakly correlated detections, whereas March 2020 contained a small subset with high *ccc* located several kilometers from the mainshock (Text S5 and Figures S24–S28 in Supporting Information S1).

6. Discussion

We show that combining the waveform recordings of surface stations with borehole seismic stations, plus employing modern automated waveform detection and processing techniques can substantially advance the detection and monitoring of low magnitude seismic processes. By integrating deep-learning based phase picking, a novel phase associator and probabilistic relocation with classical and waveform-based analyses, we obtained a denser and more homogeneous catalog of microseismic activity framing moderate earthquakes. In the following, we evaluate in more detail the importance of the borehole instrumentation to monitor low-magnitude seismicity. Furthermore, we utilize our enhanced data base of small-scale seismicity and their in-depth analysis to critically assess the seismicity patterns preceding the $M_L \geq 4$ earthquakes in the Çınarcık and the Central basins in the Sea of Marmara.

6.1. The Role of Borehole Stations in Improving the Seismicity Catalog

Borehole-based seismic monitoring has long been used to record waveforms under low noise and improve the detectability of weak, high-frequency signals. For example, at Anza near the San Jacinto Fault in Southern California, direct comparisons between surface and downhole recordings demonstrated lower ambient noise and a broader usable frequency range at depth (Aster & Shearer, 1991). At the San Andreas Fault near Parkfield, the borehole High-Resolution Seismic Network provided the basis for resolving clustered and repeating micro-earthquakes and their spatial and temporal evolution (R. Nadeau et al., 1994; R. M. Nadeau et al., 1995; Waldhauser et al., 2004), while subsequent template-matching reprocessing produced a substantially denser catalog (Neves et al., 2023). Similarly, the predominantly borehole-based Japanese Hi-net improved micro-earthquake detection and supported high-resolution analyses of crustal seismicity across Japan (Obara et al., 2005; Yano et al., 2017). These studies show that borehole observations not only lower detection thresholds but also improve the resolution of spatiotemporal seismicity patterns.

In the Marmara region, GONAF applies this established concept, where nearby surface stations are exposed to substantial anthropogenic noise due to the nearby Istanbul metropolitan region. A central result of our study is the clear performance advantage of borehole stations over surface stations for monitoring microseismicity in the densely populated Istanbul-Marmara region that exhibits substantial anthropogenic noise levels. GONAF borehole stations consistently exhibit lower day-to-night pick ratios (Figure S3 in Supporting Information S1) and reduced sensitivity to cultural noise compared to nearby surface sites, which directly translates into more stable detection conditions (Figures 3a and 3b) and a low completeness magnitude of $M_c = 0.90$ for the combined catalog within the GONAF monitoring area. A regional estimate of the magnitude of completeness is used here because the individual sequences contain too few events to adequately sample the frequency-magnitude distribution and constrain their own completeness.

Across the analyzed sequences, the GONAF borehole sensors provide the cleanest waveforms and highest *ccc* values, enabling the detection of clusters of highly similar earthquakes that are not or barely visible at surface stations. These observations corroborate previous findings that borehole installations can lower detection thresholds by up to roughly one magnitude unit (Bohnhoff et al., 2018) and can capture high-frequency wave fields that are attenuated or contaminated at the surface (e.g., Bohnhoff, Dresen, et al., 2017; Kılıç et al., 2020). Furthermore, they align with previous experience that borehole arrays increase the detectability of similar

21699356, 2026, 10, Downloaded from https://agupubs.onlinelibrary.wiley.com/doi/10.1029/2026JB034241 by Universitatsbibliothek RWTH Aachen University, Wiley Online Library on [05/11/2026]. See the Terms and Conditions (https://onlinelibrary.wiley.com/terms-and-conditions) on Wiley Online Library for rules of use; OA articles are governed by the applicable Creative Commons License

earthquakes and subtle changes in seismicity rates (Shearer & Abercrombie, 2021; Shearer & Shakibay Senobari, 2025).

However, the catalog gain nevertheless remains conditional on the PyOcto association settings, and relaxing pick and station requirements increases event counts but also produces more spatially scattered seismicity (Münchmeyer, 2024). Synthetic benchmark tests further show that suitable tolerance values vary with travel-time noise, event rate, and source-station geometry (Puente Huerta et al., 2025). We therefore required phase and station redundancy and checked the associations against GaMMA, the manually analyzed June 2016 sequence, and the merged reference catalog. These checks constrain gross association failures but do not make events near the adopted thresholds parameter invariant. The spatial interpretation is also conditional on the adopted layered 1-D velocity model by Karabulut et al. (2011) and Becker et al. (2023a, 2023b). Empirical station terms reduce average station-path residuals but cannot account for source-dependent 3-D basin heterogeneity, which can bias absolute hypocenters in the Marmara region. To reduce the influence of errors shared by nearby ray paths, our fine-scale spatial interpretation primarily relies on relative locations.

6.2. Variability in the Seismicity Patterns Preceding the Analyzed M > 4 Marmara Sequences

For the six analyzed seismic sequences, we found substantial variability in seismicity pattern behavior preceding the mainshocks (days before the main rupture). On one hand, in the Çınarcık Basin, the June 2016 M_L 4.5 sequence showed a pronounced space-time localization of the seismicity starting roughly 30–20 hr before the mainshock, quantified with the increase in waveform similarity and the microseismic activity confined to a local fault patch, thus extending the findings of previous manual analysis (Malin et al., 2018). The monotonic increase in waveform similarity and decrease in inter-event distances make this sequence the clearest example of seismicity localization in our data set. On the other hand, the other sequences located near the borehole array show very limited to no seismic activity prior to the mainshocks. The July 2016 M_L 4.0 earthquake, only about 2 km away from the June 2016 mainshock in the Çınarcık Basin, provides an important contrast to the findings above, with very limited evidence of seismicity localization. For the June and July 2016 sequences, 62 common stations are available and noise levels are comparable (Figures S4–S6 in Supporting Information S1), suggesting that the observed seismicity pattern differences are unlikely to be driven by variations in station availability.

One possibility to explain the different seismicity patterns before these mainshocks is, that the June 2016 M_L 4.5 mainshock, which was followed by a slow-slip episode on the same fault section (Durand et al., 2022; Martínez-Garzón et al., 2019), could have smoothed the local fault patch, suppressing heterogeneities that are typically activated in the occurrence of foreshocks. This could have reduced the occurrence of seismic activity before the subsequent July 2016 M_L 4.0 event. The very small epicentral distance between the June and July mainshocks raises the possibility that the June sequence had already reactivated and partially relaxed the local asperity, so that the July 2016 earthquake could nucleate on a smoother and more uniformly loaded patch without generating a comparable occurrence of seismicity prior to the mainshock.

The September 2019 earthquake sequence in the Central Basin exhibited increased activity before both the M_L 4.7 foreshock and the M_L 5.8 mainshock. We note that this sequence was monitored at a somewhat larger detection threshold given the larger epicentral distance compared to the Çınarcık sequences. Clusters in the cross-correlation matrices and elevated plateaus in the running average of the cross-correlation coefficients indicate episodes of elevated waveform similarity before each of the two Central Basin/Silivri events. Compared with the June 2016 sequence, the spatial pattern is more heterogeneous, with no monotonic approach toward the M_L 5.8 mainshock and only a weak waveform similarity between the final preceding events and the mainshock. These episodes of clustering may be viewed in the context of the two-scale preparation process proposed by Durand et al. (2020), involving a days-long activation along the future rupture followed by a short-term concentration of seismicity around the eventual epicenters. This sequence occurred in the Central Basin, where geodetic and seismological studies document significant aseismic creep on parts of the MMF shear zone (Becker et al., 2023a, 2023b), suggesting that the seismic activity may be more broadly distributed there than along the fully locked Princes' Islands segment bounding the Çınarcık Basin to the north.

The other three mainshocks in the Çınarcık Basin show no or only weak evidence of immediate seismicity and earthquake localization before the mainshocks (Figures S24–S28 in Supporting Information S1). This variability in the detectable seismicity preceding moderate earthquakes suggests that local fault conditions, prior slow slip

21699356, 2026, 10, Downloaded from https://agupubs.onlinelibrary.wiley.com/doi/10.1029/2026JB034241 by Universitatsbibliothek RWTH Aachen University, Wiley Online Library on [05/11/2026]. See the Terms and Conditions (https://onlinelibrary.wiley.com/terms-and-conditions) on Wiley Online Library for rules of use; OA articles are governed by the applicable Creative Commons License

and stress history, may control the emergence of pre-mainshock clustering in this area more strongly than large scale tectonics alone.

What is different in the June 2016 and September 2019 earthquake sequences with respect to the other four analyzed sequences to display the observed pre-mainshock clustering? There are a few possibilities, including the following: a) Structural heterogeneity. Both earthquake sequences occur near fault junctions, suggesting that these events could have ruptured more heterogeneous (rough) fault portions that did not rupture recently, containing larger structural heterogeneities and leading to more foreshocks. This effect is also observed on laboratory faults where rough fault tend to produce stronger activity (Wang et al., 2024). b) Aseismic slip. Both earthquake sequences occur near transitions between more strongly locked and more creeping fault sections (Becker et al., 2023a, 2023b; Bohnhoff et al., 2013). The occurrence of aseismic slip in the vicinity of these mainshocks could have promoted enhanced seismic activity preceding the mainshock.

Viewed in a wider context, our observations fit into the ongoing debate on whether foreshocks (or more broadly, seismicity before mainshocks) mainly reflect cascade triggering within a self-similar seismicity process or active preparation driven by aseismic slip and related processes (Martínez-Garzón & Poli, 2024; Mignan, 2014). Our results illustrate this variability: some sequences, such as June 2016 in the Çınarcık Basin, show pronounced seismicity localization, whereas others, even in close proximity, show more heterogeneous or sparse clustering. These patterns are compatible with more than one triggering or loading process.

7. Conclusions

The integrated application of deep-learning-based phase picking, advanced phase association, and probabilistic relocation techniques combined with borehole and surface waveform continuous recordings provide a consistent framework to monitor seismic deformation along the Main Marmara Fault shear zone offshore Istanbul in NW Türkiye. The main conclusions of this study are:

1. The joint use of machine learning and robust traditional seismological techniques yields a highly complete and internally consistent seismicity catalog for the Sea of Marmara. Compared to existing regional catalogs based on conventional processing, our workflow increases the number of well-located events before and after $M > 4$ mainshocks by a factor of about eight for the region inside the borehole network.
2. Borehole seismic stations from the GONAF network remarkably improve monitoring capabilities compared to surface networks alone. Their low-noise environment lowers the detection threshold, increases signal-to-noise ratios, and reduces the fraction of false or ambiguous picks, which in turn improves event associability and decreases the magnitude of completeness within the borehole monitoring area.
3. Systematic waveform cross-correlation, earthquake relocation and template matching reveal sequence-dependent seismicity clustering before the mainshocks. The June 2016 Çınarcık sequence shows the clearest localization, with sustained increases in cross-correlation coefficients and reduced inter-event distances. In the September 2019 Central Basin sequence, highly similar event families occur within a more heterogeneous spatial pattern. In contrast, nearby comparable sequences in the Çınarcık Basin, exhibit weak or no seismicity and do not show a comparable build-up of waveform similarity. This suggests that local fault state, stress history and rupture dynamics modulate the occurrence of pre-mainshock clustering.
4. Waveform similarity, earthquake relocation and template-matching analyses at borehole stations provide sensitive tools for tracking changes in microseismic activity, earthquake localization processes, and offer possibilities to be applied in real-time. However, the predictive potential of these methods is still limited due to the strong variability observed in the analysed sequences.

Conflict of Interest

The authors declare no conflicts of interest relevant to this study.

Availability Statement

The seismicity catalog generated in this study is available at GFZ Data Services (Fabisch et al., 2026). Continuous waveform data were obtained from TU (Disaster and Emergency Management Authority, 1990) through the TDVMS portal (https://tdvms.afad.gov.tr/continuous_data), KO (Kandilli Observatory And Earthquake

21699356, 2026, 10, Downloaded from https://agupubs.onlinelibrary.wiley.com/doi/10.1029/2026JB034241 by Universitatsbibliothek RWTH Aachen University, Wiley Online Library on [05/11/2026]. See the Terms and Conditions (https://onlinelibrary.wiley.com/terms-and-conditions) on Wiley Online Library for rules of use; OA articles are governed by the applicable Creative Commons License

Research Institute, Boğaziçi University, 1971) through FDSN web services, and GF (GFZ Helmholtz Centre For Geosciences & Disaster And Emergency Management Presidency, 2013) through FDSN web services. Restricted GF data can be accessed using an EIDA token, which can be requested at https://geofon.gfz.de/waveform/access/. Reference seismicity data were obtained from Becker et al. (2023a), with additional catalogs directly downloaded from AFAD (https://deprem.afad.gov.tr/event-catalog) and KOERI (http://www.koeri.boun.edu.tr/sismo/2/earthquake-catalog). Data were processed with ObsPy (Beyreuther et al., 2010; Krischer et al., 2015, https://github.com/obspy/obspy). Phase picking was performed with PhaseNet (Zhu & Beroza, 2019, https://github.com/AI4EPS/PhaseNet) integrated within SeisBench (Woollam et al., 2022, https://github.com/seisbench/seisbench), phase association with PyOcto (Münchmeyer, 2024, https://github.com/yetinam/pyocto), earthquake location with NonLinLoc (Lomax et al., 2000; Lomax et al., 2014, https://github.com/ut-beg-texnet/NonLinLoc), relative relocation with GrowClust3D.jl (Trugman & Shearer, 2017; Trugman et al., 2022, https://github.com/dttrugman/GrowClust3D.jl), and template matching with EQcorrscan (Chamberlain et al., 2017, https://github.com/eqcorrscan/eqcorrscan). Figures were created using Matplotlib (Hunter, 2007, https://github.com/matplotlib/matplotlib), and Figure 1 was created using PyGMT (Tian et al., 2025).

Acknowledgments

O.F. and P.M.G. are funded by the European Research Council (ERC) Starting Grant 101076119 (QUAKEHUNTER). We thank our colleagues from AFAD, Ankara, for the long-standing collaboration providing the basis for this study. In particular, we thank Filiz Tuba Kadirioğlu, Recai Kartal and Tuğbay Kılıç for fruitful discussions and long-term operation of the GONAF downhole seismic observatory. We thank the Editor Rachel Abercrombie, an anonymous Associate Editor, Fatih Bulut and an anonymous reviewer for their constructive suggestions and editorial comments that contributed to improve the manuscript. Open Access funding enabled and organized by Projekt DEAL.

References

Abercrombie, R. E., Chen, X., & Zhang, J. (2020). Repeating earthquakes with remarkably repeatable ruptures on the San Andreas Fault at parkfield. *Geophysical Research Letters*, *47*(23), e2020GL089820. https://doi.org/10.1029/2020GL089820

Abercrombie, R. E., & Mori, J. (1996). Occurrence patterns of foreshocks to large earthquakes in the Western United States. *Nature*, *381*(6580), 303–307. https://doi.org/10.1038/381303a0

Aster, R. C., & Shearer, P. M. (1991). High-frequency borehole seismograms recorded in the San Jacinto fault zone, Southern California. Part 2: Attenuation and site effects. *Bulletin of the Seismological Society of America*, *81*(4), 1081–1100. https://doi.org/10.1785/BSSA0810041081

Becker, D., Martínez-Garzón, P., Wollin, C., Kılıç, T., & Bohnhoff, M. (2023a). Homogenized regional seismicity catalogue for the Marmara region, northwestern Turkey, for the time interval 2006–2020 [Dataset]. *GFZ Data Services*. https://doi.org/10.5880/GFZ.4.2.2023.002

Becker, D., Martínez-Garzón, P., Wollin, C., Kılıç, T., & Bohnhoff, M. (2023b). Variation of fault creep along the overdue istanbul-marmara seismic gap in NW Türkiye. *Geophysical Research Letters*, *50*(6), e2022GL101471. https://doi.org/10.1029/2022GL101471

Becker, D., McBrearty, I. W., Beroza, G. C., & Martínez-Garzón, P. (2024). Performance of AI-Based phase picking and event association methods after the large 2023 Mw 7.8 and 7.6 Türkiye doublet. *Bulletin of the Seismological Society of America*, *114*(5), 2457–2473. https://doi.org/10.1785/0120240017

Beroza, G. C., Segou, M., & Mostafa Mousavi, S. (2021). Machine learning and earthquake forecasting—next steps. *Nature Communications*, *12*(1), 4761. https://doi.org/10.1038/s41467-021-24952-6

Beyreuther, M., Barsch, R., Krischer, L., Megies, T., Behr, Y., & Wassermann, J. (2010). ObsPy: A python toolbox for seismology. *Seismological Research Letters*, *81*(3), 530–533. https://doi.org/10.1785/gssrl.81.3.530

Bohnhoff, M. (2026). Rethinking the main Marmara Fault—seismotectonic complexity and seismic hazard in the Istanbul–Marmara region. *Geophysical Journal International*, *246*(3), ggag253. https://doi.org/10.1093/gji/ggag253

Bohnhoff, M., Bulut, F., Dresen, G., Malin, P. E., Eken, T., & Aktar, M. (2013). An earthquake gap south of Istanbul. *Nature Communications*, *4*(1), 1999. https://doi.org/10.1038/ncomms2999

Bohnhoff, M., Dresen, G., Ceken, U., Kadirioglu, F. T., Kartal, R. F., Kılıç, T., et al. (2017). GONAF – The borehole geophysical observatory at the north anatolian fault in the eastern Sea of Marmara. *Scientific Drilling*, *22*, 19–28. https://doi.org/10.5194/sd-22-19-2017

Bohnhoff, M., Malin, P. E., ter Heege, J., Deflandre, J.-P., & Sicking, C. (2018). Suggested best practice for seismic monitoring and characterization of non-conventional reservoirs. *First Break*, *36*(2), 59–64. https://doi.org/10.3997/1365-2397.n0070

Bohnhoff, M., Martínez-Garzón, P., Bulut, F., Stierle, E., & Ben-Zion, Y. (2016). Maximum earthquake magnitudes along different sections of the North Anatolian fault zone. *Tectonophysics*, *674*, 147–165. https://doi.org/10.1016/j.tecto.2016.02.028

Bohnhoff, M., Wollin, C., Domigall, D., Küperkoch, L., Martínez-Garzón, P., Kwiatek, G., et al. (2017). Repeating Marmara Sea earthquakes: Indication for fault creep. *Geophysical Journal International*, *210*(1), 332–339. https://doi.org/10.1093/gji/ggx169

Bormann, P., & Dewey, J. W. (2014). The new IASPEI standards for determining magnitudes from digital data and their relation to classical magnitudes. *New Manual of Seismological Observatory Practice*, *2*(NMSOP-2). https://doi.org/10.2312/GFZ.NMSOP-2_IS_3.3

Bouchon, M., Karabulut, H., Aktar, M., Özalaybey, S., Schmittbuhl, J., & Bouin, M.-P. (2011). Extended nucleation of the 1999 Mw 7.6 Izmit earthquake. *Science*, *331*(6019), 877–880. https://doi.org/10.1126/science.1197341

Bozkurt, E. (2001). Neotectonics of Turkey – A synthesis. *Geodinamica Acta*, *14*(1–3), 3–30. https://doi.org/10.1080/09853111.2001.11432432

Bulut, F., Bohnhoff, M., Eken, T., Janssen, C., Kılıç, T., & Dresen, G. (2012). The East Anatolian Fault Zone: Seismotectonic setting and spatiotemporal characteristics of seismicity based on precise earthquake locations. *Journal of Geophysical Research*, *117*(B7). https://doi.org/10.1029/2011JB008966

Cabrera, L., Poli, P., & Frank, W. B. (2022). Tracking the spatio-temporal evolution of foreshocks preceding the Mw 6.1 2009 L'Aquila earthquake. *Journal of Geophysical Research: Solid Earth*, *127*(3), e2021JB023888. https://doi.org/10.1029/2021JB023888

Chamberlain, C. J., Hopp, C. J., Boese, C. M., Warren-Smith, E., Chambers, D., Chu, S. X., et al. (2017). EQcorrscan: Repeating and near-repeating earthquake detection and analysis in python. *Seismological Research Letters*, *89*(1), 173–181. https://doi.org/10.1785/0220170151

Chen, X., Martínez-Garzón, P., Kwiatek, G., Ben-Zion, Y., Bohnhoff, M., & Cotton, F. (2025). Rupture directivity of moderate earthquakes along the main marmara fault suggests larger ground motion towards Istanbul. *Geophysical Research Letters*, *52*(1), e2024GL111460. https://doi.org/10.1029/2024GL111460

Chen, X., & Shearer, P. M. (2016). Analysis of foreshock sequences in California and implications for earthquake triggering. *Pure and Applied Geophysics*, *173*(1), 133–152. https://doi.org/10.1007/s00024-015-1103-0

Crowley, H., Dabbeek, J., Despotaki, V., Rodrigues, D., Martins, L., Silva, V., et al. (2021). European Seismic Risk Model (ESRM20). Tech. Rep. *Eucentre*. https://doi.org/10.3929/ethz-b-000590388

Cui, X., Li, Z., Ampuero, J.-P., & De Barros, L. (2025). Does foreshock identification depend on seismic monitoring capability? *Geophysical Research Letters*, *52*(11), e2025GL115394. https://doi.org/10.1029/2025GL115394

Delorey, A. A., Guyer, R. A., Bokelmann, G. H. R., & Johnson, P. A. (2021). Probing the damage zone at parkfield. *Geophysical Research Letters*, *48*(13), e2021GL093518. https://doi.org/10.1029/2021GL093518

Dieterich, J. H. (1992). Earthquake nucleation on faults with rate-and state-dependent strength. *Tectonophysics*, *211*(1), 115–134. https://doi.org/10.1016/0040-1951(92)90055-B

Disaster and Emergency Management Authority. (1990). Turkish national seismic network [Dataset]. *Department of Earthquake, Disaster and Emergency Management Authority*. https://doi.org/10.7914/SN/TU

Durand, V., Bentz, S., Kwiatek, G., Dresen, G., Wollin, C., Heidbach, O., et al. (2020). A two-scale preparation phase preceded an Mw 5.8 earthquake in the Sea of Marmara offshore istanbul. *Turkey. Seismological Research Letters*, *91*(6), 3139–3147. https://doi.org/10.1785/0220200110

Durand, V., Gualandi, A., Ergintav, S., Kwiatek, G., Haghshenas, M., Motagh, M., et al. (2022). Deciphering aseismic deformation along submarine fault branches below the eastern Sea of Marmara (Turkey): Insights from seismicity, strainmeter, and GNSS data. *Earth and Planetary Science Letters*, *594*, 117702. https://doi.org/10.1016/j.epsl.2022.117702

Ellsworth, W. L., & Beroza, G. C. (1995). Seismic evidence for an earthquake nucleation phase. *Science*, *268*(5212), 851–855. https://doi.org/10.1126/science.268.5212.851

Ellsworth, W. L., & Bulut, F. (2018). Nucleation of the 1999 Izmit earthquake by a triggered cascade of foreshocks. *Nature Geoscience*, *11*(7), 531–535. https://doi.org/10.1038/s41561-018-0145-1

Ergintav, S., Reilinger, R. E., Çakmak, R., Floyd, M., Cakir, Z., Doğan, U., et al. (2014). Istanbul's earthquake hot spots: Geodetic constraints on strain accumulation along faults in the Marmara seismic gap. *Geophysical Research Letters*, *41*(16), 5783–5788. https://doi.org/10.1002/2014GL060985

Fabisch, O., Bohnhoff, M., & Martínez-Garzón, P. (2026). Sequence-based seismicity catalog for the Sea of Marmara (NW Türkiye), 2016–2023 [Dataset]. *GFZ Data Services*. https://doi.org/10.5880/gfz.itsj.2026.001

Flerit, F., Armijo, R., King, G., & Meyer, B. (2004). The mechanical interaction between the propagating North Anatolian Fault and the back-arc extension in the Aegean. *Earth and Planetary Science Letters*, *224*(3), 347–362. https://doi.org/10.1016/j.epsl.2004.05.028

GFZ Helmholtz Centre For GeosciencesDisaster And Emergency Management Presidency. (2013). Geophysical borehole observatory at the north anatolian fault (GONAF) [Dataset]. *GFZ Data Services*. https://doi.org/10.14470/TS373432

Gomberg, J. (2018). Unsettled earthquake nucleation. *Nature Geoscience*, *11*(7), 463–464. https://doi.org/10.1038/s41561-018-0149-x

Grund, M., Groos, J. C., & Ritter, J. R. R. (2016). Fault reactivation analysis using microearthquake clustering based on signal-to-noise weighted waveform similarity. *Pure and Applied Geophysics*, *173*(7), 2325–2355. https://doi.org/10.1007/s00024-016-1281-4

Guvercin, S. E., & Barbot, S. (2025). Persistent rupture segmentation of the Main Marmara Fault. *Communications Earth & Environment*, *6*(1), 1028. https://doi.org/10.1038/s43247-025-03007-4

Helmstetter, A., & Sornette, D. (2003). Foreshocks explained by cascades of triggered seismicity. *Journal of Geophysical Research*, *108*(B10), 2457. https://doi.org/10.1029/2003JB002409

Hergert, T., & Heidbach, O. (2010). Slip-rate variability and distributed deformation in the Marmara Sea fault system. *Nature Geoscience*, *3*(2), 132–135. https://doi.org/10.1038/ngeo739

Hunter, J. D. (2007). Matplotlib: A 2D graphics environment. *Computing in Science & Engineering*, *9*(3), 90–95. https://doi.org/10.1109/MCSE.2007.55

Isken, M., Niemz, P., Münchmeyer, J., Büyükakpınar, P., Heimann, S., Cesca, S., & Dahm, T. (2025). Qseek: A data-driven framework for automated earthquake detection, localization and characterization. *Seismica*, *4*(1). https://doi.org/10.26443/seismica.v4i1.1283

Jiang, C., Fang, L., Fan, L., & Li, B. (2021). Comparison of the earthquake detection abilities of PhaseNet and EQTransformer with the Yangbi and Maduo earthquakes. *Earthquake Science*, *34*(5), 425–435. https://doi.org/10.29382/eqs-2021-0038

Johnson, C. W., & Johnson, P. A. (2021). Learning the low frequency earthquake activity on the central San Andreas Fault. *Geophysical Research Letters*, *48*(13), e2021GL092951. https://doi.org/10.1029/2021GL092951

Jolivet, L., Faccenna, C., Huet, B., Labrousse, L., Le Pourhiet, L., Lacombe, O., et al. (2013). Aegean tectonics: Strain localisation, slab tearing and trench retreat. *Tectonophysics*, *597–598*, 1–33. https://doi.org/10.1016/j.tecto.2012.06.011

Jones, L. M., & Molnar, P. (1979). Some characteristics of foreshocks and their possible relationship to earthquake prediction and premonitory slip on faults. *Journal of Geophysical Research*, *84*(B7), 3596–3608. https://doi.org/10.1029/JB084iB07p03596

Kanamori, H. (1981). The nature of seismicity patterns before large earthquakes. In *Earthquake prediction* (pp. 1–19). American Geophysical Union (AGU). https://doi.org/10.1029/ME004p0001

Kandilli Observatory And Earthquake Research Institute, Boğaziçi University. (1971). Kandilli observatory and earthquake research institute (KOERI) [Dataset]. *International Federation of Digital Seismograph Networks*. https://doi.org/10.7914/SN/KO

Karabulut, H., Schmittbuhl, J., Özalaybey, S., Lengliné, O., Kömeç-Mutlu, A., Durand, V., et al. (2011). Evolution of the seismicity in the eastern Marmara Sea a decade before and after the 17 August 1999 Izmit earthquake. *Tectonophysics*, *510*(1), 17–27. https://doi.org/10.1016/j.tecto.2011.07.009

Karimpouli, S., Caus, D., Grover, H., Martínez-Garzón, P., Bohnhoff, M., Beroza, G. C., et al. (2023). Explainable machine learning for labquake prediction using catalog-driven features. *Earth and Planetary Science Letters*, *622*, 118383. https://doi.org/10.1016/j.epsl.2023.118383

Karimpouli, S., Kwiatek, G., Ben-Zion, Y., Martínez-Garzón, P., Dresen, G., & Bohnhoff, M. (2024). Empowering machine learning forecasting of labquake using event-based features and clustering characteristics. *Journal of Geophysical Research: Machine Learning and Computation*, *1*(2), e2024JH000160. https://doi.org/10.1029/2024JH000160

Karimpouli, S., Kwiatek, G., Martínez-Garzón, P., Caus, D., Wang, L., Dresen, G., & Bohnhoff, M. (2025). Forecasting induced seismicity in enhanced geothermal systems using machine learning: Challenges and opportunities. *Geophysical Journal International*, *242*(2), ggaf155. https://doi.org/10.1093/gji/ggaf155

Kato, A., & Ben-Zion, Y. (2021). The generation of large earthquakes. *Nature Reviews Earth & Environment*, *2*(1), 26–39. https://doi.org/10.1038/s43017-020-00108-w

Khan, R. A., Werner, M. J., Biggs, J., & Fagereng, Å. (2025). Effect of mainshock selection, earthquake catalog and definition on foreshock rate estimates in Southern California. *Journal of Geophysical Research: Solid Earth*, *130*(7), e2024JB030733. https://doi.org/10.1029/2024JB030733

Kılıç, T., Kartal, R. F., Kadirioğlu, F. T., Bohnhoff, M., Nurlu, M., Acarel, D., et al. (2020). Geophysical borehole observatory at the north anatolian fault in the Eastern Sea of Marmara (GONAF): Initial results. *Journal of Seismology*, *24*(2), 375–395. https://doi.org/10.1007/s10950-020-09907-6

Kılıç, T., Ottemöller, L., Havskov, J., Yanık, K., Kılıçarslan, Ö., Alver, F., & Özyazıcıoğlu, M. (2017). Local magnitude scale for earthquakes in Turkey. *Journal of Seismology*, *21*(1), 35–46. https://doi.org/10.1007/s10950-016-9581-9

21699356, 2026, 10, Downloaded from https://agupubs.onlinelibrary.wiley.com/doi/10.1029/2026JB034241 by Universitatsbibliothek RWTH Aachen University, Wiley Online Library on [05/11/2026]. See the Terms and Conditions (https://onlinelibrary.wiley.com/terms-and-conditions) on Wiley Online Library for rules of use; OA articles are governed by the applicable Creative Commons License

Krischer, L., Megies, T., Barsch, R., Beyreuther, M., Lecocq, T., Caudron, C., & Wassermann, J. (2015). Obspy: A bridge for seismology into the scientific python ecosystem. *Computational Science & Discovery*, *8*(1), 014003. https://doi.org/10.1088/1749-4699/8/1/014003

Kwiatek, G., Martínez-Garzón, P., Goebel, T., Bohnhoff, M., Ben-Zion, Y., & Dresen, G. (2024). Intermittent criticality multi-scale processes leading to large slip events on rough laboratory faults. *Journal of Geophysical Research: Solid Earth*, *129*(3), e2023JB028411. https://doi.org/10.1029/2023JB028411

Le Pichon, X., Şengör, A., Demirbağ, E., Rangin, C., İmren, C., Armijo, R., et al. (2001). The active Main Marmara Fault. *Earth and Planetary Science Letters*, *192*(4), 595–616. https://doi.org/10.1016/S0012-821X(01)00449-6

Le Pichon, X., Şengör, A. M. C., Kende, J., İmren, C., Henry, P., Grall, C., & Karabulut, H. (2016). Propagation of a strike-slip plate boundary within an extensional environment: The westward propagation of the North Anatolian Fault. *Canadian Journal of Earth Sciences*, *53*(11), 1416–1439. https://doi.org/10.1139/cjes-2015-0129

Lomax, A., Michelini, A., & Curtis, A. (2014). Earthquake location, direct, global-search methods. In R. A. Meyers (Ed.), *Encyclopedia of complexity and systems science* (pp. 1–33). Springer New York. https://doi.org/10.1007/978-3-642-27737-5_150-2

Lomax, A., Virieux, J., Volant, P., & Berge-Thierry, C. (2000). Probabilistic earthquake location in 3D and layered models. In C. H. Thurber & N. Rabinowitz (Eds.), *Advances in seismic event location* (pp. 101–134). Springer Netherlands. https://doi.org/10.1007/978-94-015-9536-0_5

Malin, P. E., Bohnhoff, M., Blümle, F., Dresen, G., Martínez-Garzón, P., Nurlu, M., et al. (2018). Microearthquakes preceding a M4.2 Earthquake Offshore Istanbul. *Scientific Reports*, *8*(1), 16176. https://doi.org/10.1038/s41598-018-34563-9

Martínez-Garzón, P., Becker, D., Jara, J., Chen, X., Kwiatek, G., & Bohnhoff, M. (2023). The 2022 MW 6.0 Gölyaka–Düzce earthquake: An example of a medium-sized earthquake in a fault zone early in its seismic cycle. *Solid Earth*, *14*(10), 1103–1121. https://doi.org/10.5194/se-14-1103-2023

Martínez-Garzón, P., Beroza, G. C., Bocchini, G. M., & Bohnhoff, M. (2023). Sea level changes affect seismicity rates in a hydrothermal system near Istanbul. *Geophysical Research Letters*, *50*(3), e2022GL101258. https://doi.org/10.1029/2022GL101258

Martínez-Garzón, P., Bohnhoff, M., Mencin, D., Kwiatek, G., Dresen, G., Hodgkinson, K., et al. (2019). Slow strain release along the eastern Marmara region offshore Istanbul in conjunction with enhanced local seismic moment release. *Earth and Planetary Science Letters*, *510*, 209–218. https://doi.org/10.1016/j.epsl.2019.01.001

Martínez-Garzón, P., Chen, X., Becker, D., Núñez-Jara, S., Kartal, R. F., Türker, E., et al. (2026). Progressive eastward rupture of the Main Marmara fault toward Istanbul. *Science*, *391*(6783), 379–383. https://doi.org/10.1126/science.adz0072

Martínez-Garzón, P., & Poli, P. (2024). Cascade and pre-slip models oversimplify the complexity of earthquake preparation in nature. *Communications Earth & Environment*, *5*(1), 120. https://doi.org/10.1038/s43247-024-01285-y

McBrearty, I. W., & Beroza, G. C. (2023). Earthquake phase association with graph neural networks. *Bulletin of the Seismological Society of America*, *113*(2), 524–547. https://doi.org/10.1785/0120220182

McClusky, S., Balassanian, S., Barka, A., Demir, C., Ergintav, S., Georgiev, I., et al. (2000). Global Positioning System constraints on plate kinematics and dynamics in the eastern Mediterranean and Caucasus. *Journal of Geophysical Research*, *105*(B3), 5695–5719. https://doi.org/10.1029/1999JB900351

Michelini, A., Cianetti, S., Gaviano, S., Giunchi, C., Jozinović, D., & Lauciani, V. (2021). INSTANCE the Italian seismic dataset for machine learning [Dataset]. *Istituto Nazionale di Geofisica e Vulcanologia (INGV)*. https://doi.org/10.13127/INSTANCE

Mignan, A. (2014). The debate on the prognostic value of earthquake foreshocks: A meta-analysis. *Scientific Reports*, *4*(1), 4099. https://doi.org/10.1038/srep04099

Mousavi, S. M., & Beroza, G. C. (2022). Deep-learning seismology. *Science*, *377*(6607), eabm4470. https://doi.org/10.1126/science.abm4470

Mousavi, S. M., Ellsworth, W. L., Zhu, W., Chuang, L. Y., & Beroza, G. C. (2020). Earthquake transformer—An attentive deep-learning model for simultaneous earthquake detection and phase picking. *Nature Communications*, *11*(1), 3952. https://doi.org/10.1038/s41467-020-17591-w

Mousavi, S. M., Sheng, Y., Zhu, W., & Beroza, G. C. (2019). STanford EArthquake dataset (STEAD): A global data set of seismic signals for AI. *IEEE Access*, *7*, 179464–179476. https://doi.org/10.1109/ACCESS.2019.2947848

Moutote, L., Marsan, D., Lengliné, O., & Duputel, Z. (2021). Rare occurrences of non-cascading foreshock activity in Southern California. *Geophysical Research Letters*, *48*(7), e2020GL091757. https://doi.org/10.1029/2020GL091757

Münchmeyer, J. (2024). PyOcto: A high-throughput seismic phase associator. *Seismica*, *3*(1). https://doi.org/10.26443/seismica.v3i1.1130

Murru, M., Akinci, A., Falcone, G., Pucci, S., Console, R., & Parsons, T. (2016). M≥ 7 earthquake rupture forecast and time-dependent probability for the Sea of Marmara region, Turkey. *Journal of Geophysical Research: Solid Earth*, *121*(4), 2679–2707. https://doi.org/10.1002/2015JB012595

Nadeau, R., Antolik, M., Johnson, P. A., Foxall, W., & McEvilly, T. V. (1994). Seismological studies at Parkfield III: Microearthquake clusters in the study of fault-zone dynamics. *Bulletin of the Seismological Society of America*, *84*(2), 247–263. https://doi.org/10.1785/BSSA0840020247

Nadeau, R. M., Foxall, W., & McEvilly, T. V. (1995). Clustering and periodic recurrence of microearthquakes on the San Andreas Fault at parkfield, California. *Science*, *267*(5197), 503–507. https://doi.org/10.1126/science.267.5197.503

Nadeau, R. M., & McEvilly, T. V. (2004). Periodic pulsing of characteristic microearthquakes on the San Andreas Fault. *Science*, *303*(5655), 220–222. https://doi.org/10.1126/science.1090353

Neves, M., Peng, Z., & Lin, G. (2023). A high-resolution earthquake catalog for the 2004 Mw 6 parkfield earthquake sequence using a matched filter technique. *Seismological Research Letters*, *94*(1), 507–521. https://doi.org/10.1785/0220220206

Northern California Earthquake Data Center. (2014). *Northern California earthquake data Center*. Northern California Earthquake Data Center. https://doi.org/10.7932/NCEDC

Obara, K., Kasahara, K., Hori, S., & Okada, Y. (2005). A densely distributed high-sensitivity seismograph network in Japan: Hi-net by national research institute for Earth science and disaster prevention. *Review of Scientific Instruments*, *76*(2), 021301. https://doi.org/10.1063/1.1854197

Öztürk, Y. K., Konca, A. Ö., & Özel, N. M. (2025). 3D dynamic rupture simulations for the potential main marmara fault earthquake in the Sea of Marmara based on the inter-seismic strain accumulation. *Journal of Geophysical Research: Solid Earth*, *130*(7), e2024JB029585. https://doi.org/10.1029/2024JB029585

Parsons, T. (2004). Recalculated probability of M≥ 7 earthquakes beneath the Sea of Marmara, Turkey. *Journal of Geophysical Research*, *109*(B5). https://doi.org/10.1029/2003JB002667

Peterson, J. (1993). (Report No. 93-322. U.S. Geological Survey. Observations and modeling of seismic background noise. https://doi.org/10.3133/ofr93322

Prevedel, B., Bulut, F., Bohnhoff, M., Raub, C., Kartal, R. F., Alver, F., & Malin, P. E. (2015). Downhole geophysical observatories: Best installation practices and a case history from Turkey. *International Journal of Earth Sciences*, *104*(6), 1537–1547. https://doi.org/10.1007/s00531-015-1147-5

Puente Huerta, J., Sippl, C., Münchmeyer, J., & McBrearty, I. W. (2025). Benchmarking seismic phase associators: Insights from synthetic scenarios. *Seismica*, *4*(2). https://doi.org/10.26443/seismica.v4i2.1559

21699356, 2026, 10, Downloaded from https://agupubs.onlinelibrary.wiley.com/doi/10.1029/2026JB034241 by Universitatsbibliothek RWTH Aachen University, Wiley Online Library on [05/11/2026]. See the Terms and Conditions (https://onlinelibrary.wiley.com/terms-and-conditions) on Wiley Online Library for rules of use; OA articles are governed by the applicable Creative Commons License

Reasenberg, P. A. (1999). Foreshock occurrence before large earthquakes. *Journal of Geophysical Research*, *104*(B3), 4755–4768. https://doi.org/10.1029/1998JB900089

Reilinger, R., McClusky, S., Vernant, P., Lawrence, S., Ergintav, S., Cakmak, R., et al. (2006). GPS constraints on continental deformation in the africa-arabia-eurasia continental collision zone and implications for the dynamics of plate interactions. *Journal of Geophysical Research*, *111*(B5). https://doi.org/10.1029/2005JB004051

Ronneberger, O., Fischer, P., & Brox, T. (2015). U-Net: Convolutional networks for biomedical image segmentation. In N. Navab, J. Hornegger, W. M. Wells, & A. F. Frangi (Eds.), *Medical image computing and computer-assisted intervention – MICCAI 2015* (pp. 234–241). Springer International Publishing.

Ross, Z. E., Meier, M.-A., Hauksson, E., & Heaton, T. H. (2018). Generalized seismic phase detection with deep learning. *Bulletin of the Seismological Society of America*, *108*(5A), 2894–2901. https://doi.org/10.1785/0120180080

Rouet-Leduc, B., Hulbert, C., Lubbers, N., Barros, K., Humphreys, C. J., & Johnson, P. A. (2017). Machine learning predicts laboratory earthquakes. *Geophysical Research Letters*, *44*(18), 9276–9282. https://doi.org/10.1002/2017GL074677

Ruina, A. (1983). Slip instability and state variable friction laws. *Journal of Geophysical Research*, *88*(B12), 10359–10370. https://doi.org/10.1029/JB088iB12p10359

Şahin, M., Yaltırak, C., Bulut, F., & Garagon, A. (2022). Stress change generated by the 2019 Istanbul–Silivri earthquakes along the complex structure of the North Anatolian Fault in the Marmara Sea. *Earth Planets and Space*, *74*(1), 167. https://doi.org/10.1186/s40623-022-01706-2

Schaff, D. P., Bokelmann, G. H. R., Ellsworth, W. L., Zanzerkia, E., Waldhauser, F., & Beroza, G. C. (2004). Optimizing correlation techniques for improved earthquake location. *Bulletin of the Seismological Society of America*, *94*(2), 705–721. https://doi.org/10.1785/0120020238

Schmittbuhl, J., Karabulut, H., Lengliné, O., & Bouchon, M. (2016). Long-lasting seismic repeaters in the Central Basin of the Main Marmara Fault. *Geophysical Research Letters*, *43*(18), 9527–9534. https://doi.org/10.1002/2016GL070505

Şengör, A. M. C. (1979). Mid-Mesozoic closure of Permo–Triassic Tethys and its implications. *Nature*, *279*(5714), 590–593. https://doi.org/10.1038/279590a0

Şengör, A. M. C., Tüysüz, O., İmren, C., Sakınç, M., Eyidoğan, H., Görür, N., et al. (2005). THE NORTH Anatolian Fault: A NEW LOOK. *Annual Review of Earth and Planetary Sciences*, *33*(33), 37–112. https://doi.org/10.1146/annurev.earth.32.101802.120415

Shearer, P. M., & Abercrombie, R. E. (2021). Calibrating spectral decomposition of local earthquakes using borehole Seismic Records—Results for the 1992 big bear aftershocks in Southern California. *Journal of Geophysical Research: Solid Earth*, *126*(3), e2020JB020561. https://doi.org/10.1029/2020JB020561

Shearer, P. M., & Shakibay Senobari, N. (2025). Continuous aftershock hum for over ten days following the 2019 Ridgecrest, California, earthquakes observed with borehole seismometers. *Seismological Research Letters*, *96*(5), 2968–2978. https://doi.org/10.1785/0220250017

Tian, D., Leong, W. J., Fröhlich, Y., Grund, M., Schlitzer, W., Jones, M., et al. (2025). PyGMT: A python interface for the generic mapping tools [Software]. *Zenodo*. https://doi.org/10.5281/zenodo.17156962

Trugman, D. T., Chamberlain, C. J., Savvaidis, A., & Lomax, A. (2022). GrowClust3D.jl: A julia package for the relative relocation of earthquake hypocenters using 3D velocity models. *Seismological Research Letters*, *94*(1), 443–456. https://doi.org/10.1785/0220220193

Trugman, D. T., & Ross, Z. E. (2019). Pervasive foreshock activity across Southern California. *Geophysical Research Letters*, *46*(15), 8772–8781. https://doi.org/10.1029/2019GL083725

Trugman, D. T., & Shearer, P. M. (2017). GrowClust: A hierarchical clustering algorithm for relative earthquake relocation, with application to the Spanish springs and Sheldon, Nevada, earthquake sequences. *Seismological Research Letters*, *88*(2A), 379–391. https://doi.org/10.1785/0220160188

van den Ende, M. P. A., & Ampuero, J.-P. (2020). On the statistical significance of foreshock sequences in Southern California. *Geophysical Research Letters*, *47*(3), e2019GL086224. https://doi.org/10.1029/2019GL086224

Waldhauser, F., Ellsworth, W. L., Schaff, D. P., & Cole, A. (2004). Streaks, multiplets, and holes: High-resolution spatio-temporal behavior of Parkfield seismicity. *Geophysical Research Letters*, *31*(18). https://doi.org/10.1029/2004GL020649

Waldhauser, F., & Schaff, D. P. (2021). A comprehensive search for repeating earthquakes in Northern California: Implications for fault creep, slip rates, slip partitioning, and transient stress. *Journal of Geophysical Research: Solid Earth*, *126*(11), e2021JB022495. https://doi.org/10.1029/2021JB022495

Wang, L., Kwiatek, G., Renard, F., Guérin-Marthe, S., Rybacki, E., Bohnhoff, M., et al. (2024). Fault roughness controls injection-induced seismicity. *Proceedings of the National Academy of Sciences*, *121*(3), e2310039121. https://doi.org/10.1073/pnas.2310039121

Wiemer, S., & Wyss, M. (2000). Minimum magnitude of completeness in earthquake catalogs: Examples from Alaska, the Western United States, and Japan. *Bulletin of the Seismological Society of America*, *90*(4), 859–869. https://doi.org/10.1785/0119990114

Woessner, J., & Wiemer, S. (2005). Assessing the quality of earthquake catalogues: Estimating the magnitude of completeness and its uncertainty. *Bulletin of the Seismological Society of America*, *95*(2), 684–698. https://doi.org/10.1785/0120040007

Wollin, C., Bohnhoff, M., Martínez-Garzón, P., Küperkoch, L., & Raub, C. (2018). A unified earthquake catalogue for the Sea of Marmara region, Turkey, based on automatized phase picking and travel-time inversion: Seismotectonic implications. *Tectonophysics*, *747–748*, 416–444. https://doi.org/10.1016/j.tecto.2018.05.020

Wong, H. K., Lüdmann, T., Ulug, A., & Görür, N. (1995). The Sea of Marmara: A plate boundary sea in an escape tectonic regime. *Tectonophysics*, *244*(4), 231–250. https://doi.org/10.1016/0040-1951(94)00245-5

Woollam, J., Münchmeyer, J., Tilmann, F., Rietbrock, A., Lange, D., Bornstein, T., et al. (2022). SeisBench—A toolbox for machine learning in seismology. *Seismological Research Letters*, *93*(3), 1695–1709. https://doi.org/10.1785/0220210324

Yamamoto, R., Kido, M., Ohta, Y., Takahashi, N., Yamamoto, Y., Pinar, A., et al. (2019). Seafloor geodesy revealed partial creep of the north anatolian fault submerged in the Sea of Marmara. *Geophysical Research Letters*, *46*(3), 1268–1275. https://doi.org/10.1029/2018GL080984

Yamamoto, Y., Kalafat, D., Pinar, A., Takahashi, N., Coskun, Z., Polat, R., et al. (2020). Fault geometry beneath the Western and Central Marmara Sea, Turkey, based on ocean bottom seismographic observations: Implications for future large earthquakes. *Tectonophysics*, *791*, 228568. https://doi.org/10.1016/j.tecto.2020.228568

Yano, T. E., Takeda, T., Matsubara, M., & Shiomi, K. (2017). Japan unified hIgh-resolution relocated catalog for earthquakes (JUICE): Crustal seismicity beneath the Japanese Islands. *Tectonophysics*, *702*, 19–28. https://doi.org/10.1016/j.tecto.2017.02.017

Zhu, W., & Beroza, G. C. (2019). PhaseNet: A deep-neural-network-based seismic arrival-time picking method. *Geophysical Journal International*, *216*(1), 261–273. https://doi.org/10.1093/gji/ggy423

Zhu, W., McBrearty, I. W., Mousavi, S. M., Ellsworth, W. L., & Beroza, G. C. (2022). Earthquake phase association using a bayesian Gaussian mixture model. *Journal of Geophysical Research: Solid Earth*, *127*(5), e2021JB023249. https://doi.org/10.1029/2021JB023249

21699356, 2026, 10, Downloaded from https://agupubs.onlinelibrary.wiley.com/doi/10.1029/2026JB034241 by Universitatsbibliothek RWTH Aachen University, Wiley Online Library on [05/11/2026]. See the Terms and Conditions (https://onlinelibrary.wiley.com/terms-and-conditions) on Wiley Online Library for rules of use; OA articles are governed by the applicable Creative Commons License